

UC Davis

UC Davis Previously Published Works

Title

The AMIGO1 adhesion protein activates Kv2.1 voltage sensors

Permalink

<https://escholarship.org/uc/item/82r5z7d3>

Journal

Biophysical Journal, 121(8)

ISSN

0006-3495

Authors

Sepela, Rebecka J
Stewart, Robert G
Valencia, Luis A
et al.

Publication Date

2022-04-01

DOI

10.1016/j.bpj.2022.03.020

Peer reviewed

The AMIGO1 adhesion protein activates Kv2.1 voltage sensors

Rebecka J. Sepela,¹ Robert G. Stewart,¹ Luis A. Valencia,³ Parashar Thapa,¹ Zeming Wang,³ Bruce E. Cohen,^{3,4} and Jon T. Sack^{1,2,*}

¹Department of Physiology and Membrane Biology, University of California, Davis, California; ²Department of Anesthesiology and Pain Medicine, University of California, Davis, California; ³Molecular Foundry, Lawrence Berkeley National Laboratory, Berkeley, California; and ⁴Division of Molecular Biophysics & Integrated Bioimaging, Lawrence Berkeley National Laboratory, Berkeley, California

ABSTRACT Kv2 voltage-gated potassium channels are modulated by amphotericin-induced gene and open reading frame (AMIGO) neuronal adhesion proteins. Here, we identify steps in the conductance activation pathway of Kv2.1 channels that are modulated by AMIGO1 using voltage-clamp recordings and spectroscopy of heterologously expressed Kv2.1 and AMIGO1 in mammalian cell lines. AMIGO1 speeds early voltage-sensor movements and shifts the gating charge-voltage relationship to more negative voltages. The gating charge-voltage relationship indicates that AMIGO1 exerts a larger energetic effect on voltage-sensor movement than is apparent from the midpoint of the conductance-voltage relationship. When voltage sensors are detained at rest by voltage-sensor toxins, AMIGO1 has a greater impact on the conductance-voltage relationship. Fluorescence measurements from voltage-sensor toxins bound to Kv2.1 indicate that with AMIGO1, the voltage sensors enter their earliest resting conformation, yet this conformation is less stable upon voltage stimulation. We conclude that AMIGO1 modulates the Kv2.1 conductance activation pathway by destabilizing the earliest resting state of the voltage sensors.

SIGNIFICANCE Kv2 potassium channels activate a potassium conductance that shapes neuronal action potentials. The AMIGO family of adhesion proteins modulate activation of Kv2 conductances, yet, which activation steps are modified is unknown. This study finds that AMIGO1 destabilizes the earliest resting conformation of the Kv2.1 voltage sensors to promote activation of channel conductance.

INTRODUCTION

Voltage-gated potassium (Kv) channels of the Kv2 family open following membrane depolarization and are critical regulators of neuronal electrical excitability. Mammals have two Kv2 pore-forming α subunits, Kv2.1 and Kv2.2, which function as homo- or heterotetramers (1). The molecular architecture of Kv2 channels is similar to Kv1 channels for which atomic resolution structures have been solved (2). Each α -subunit monomer has six transmembrane helical segments, S1–S6. S1–S4 comprise a voltage-sensor domain (VSD), while S5 and S6 together form one quarter of the central pore domain. In response to sufficiently positive intracellular voltages, gating charges within the VSD translate from an intracellular resting position to a more extracellular activated conformation. This gating-charge

movement powers the conformational changes of voltage-sensor activation, which are coupled to subsequent pore opening and K^+ conduction (3). Kv channels progress through a landscape of conformations leading to opening, all of which define a pathway for the activation of the K^+ conductance. The activation pathway of Kv2 channels is distinct from Kv1 channels, as Kv2.1 channels have a pore-opening step that is slower and more weakly voltage-dependent than the VSD movement of Kv1 channels (3–5). The unique kinetics and voltage dependence of Kv2 currents are critical to neuronal activity as they regulate action-potential duration and can either support or limit repetitive firing (6–10).

Kv2 channels are abundant in most mammalian central neurons (11). Genetic deletion of Kv2.1 leads to seizure susceptibility and behavioral hyperexcitability in mice (12), and human Kv2.1 mutations result in developmental epileptic encephalopathy (13–15), underscoring the importance of these channels to brain function. Homeostatic Kv2.1 regulation maintains neuronal excitability (16).

Submitted July 10, 2021, and accepted for publication March 16, 2022.

*Correspondence: jsack@ucdavis.edu

Editor: Baron Chanda.

<https://doi.org/10.1016/j.bpj.2022.03.020>

© 2022 Biophysical Society.

This is an open access article under the CC BY license (<http://creativecommons.org/licenses/by/4.0/>).



Kv2.1 regulation by ischemia (17,18), glutamate (19), phosphorylation (20), and SUMOylation (21) and amphoterin-induced gene and open reading frame (AMIGO) auxiliary subunits (22,23) all shift the midpoint of the conductance-voltage relation ($G-V$). However, it is not known which steps in the conductance activation pathway are modulated by any of these forms of regulation.

To identify steps in the Kv2.1 conduction activation pathway that are susceptible to modulation, we studied the impact of an AMIGO auxiliary subunit. The AMIGO family of proteins contains three paralogs in mammals: AMIGO1, AMIGO2, and AMIGO3. AMIGO proteins are single-pass transmembrane proteins with an extracellular immunoglobulin domain and several leucine-rich repeats (24). AMIGO1 has been proposed to play a role in schizophrenia biology (25). In vertebrate brain neurons, AMIGO1 is important for cell adhesion (24), neuronal tract development (26), and circuit formation (25–27). AMIGO1 colocalizes with Kv2 in neurons throughout the brains of multiple mammalian species (22,28). Co-immunoprecipitation of AMIGO1 and Kv2.1 (22,23,26) and co-diffusion through cell membranes (22) indicate a robust interaction, consistent with an AMIGO1-Kv2.1 complex being sufficiently stable for intensive biophysical studies. All three AMIGO proteins activate the conductance of both Kv2 channel subtypes, shifting the $G-V$ by -5 to -15 mV (22,23). While these shifts may seem small in excitable cells that can have voltage swings of more than 100 mV, human mutations that shift the $G-V$ of ion-channel gating by similar magnitudes are correlated with physiological consequences (13,29–31). However, it is difficult to determine whether the physiological consequences of mutations are caused by the gating shifts themselves.

Here, we investigate which steps in the Kv2.1 conductance activation pathway are modulated by AMIGO1. In other voltage-gated ion channels, the $G-V$ relation can be shifted to more negative voltages by modulating pore opening (32–34), voltage-sensor movement (35,36), or voltage sensor-pore coupling (37–39). Single-pass transmembrane auxiliary subunits modulate other voltage-gated ion channel α subunits by a variety of mechanisms (32,38,40,41). However, AMIGO1 only shares a limited degree of homology with other single-pass transmembrane auxiliary subunits (42), and divergent structural interactions have been observed among single-pass transmembrane auxiliary subunits (43,44). As there is no consensus binding pose or mechanism of interaction for auxiliary subunits, it is difficult to predict on which step in the conductance activation pathway AMIGO1 acts. A recent study proposed that AMIGO proteins shift Kv2.1 conductance by increasing voltage sensor-pore coupling and that AMIGO-conferred changes to Kv2 voltage-sensing machinery are unlikely (23). Here, we ask whether AMIGO1 alters conformational changes associated with pore opening or with voltage-sensor movement using a combination of electrophysiological and

imaging approaches. We find that AMIGO1 modulates voltage-sensor movements that occur before pore opening. We find AMIGO1 to have a greater impact on early voltage-sensor movements than the $G-V$. We conclude that AMIGO1 destabilizes the earliest resting conformation in the pathway of channel activation.

MATERIALS AND METHODS

GxTX peptides

A conjugate of a cysteine-modified guangxitoxin-1E and the maleimide of fluorophore Alexa594 (GxTX Ser13Cys(Alexa594)) was used to selectively modulate Kv2.1 channel gating and to fluorescently identify surface-expressing Kv2.1 channels (45). Conjugates of propargylglycine (Pra)-modified GxTX and the fluorophore JP-N₃ (GxTX Ser13Pra(JP) and GxTX Lys27Pra(JP)) were used to monitor the chemical environment surrounding GxTX when localized to the channel (46). All modified GxTX mutants were synthesized by solid-phase peptide synthesis as described (46–48). Stock solutions were stored at -80°C and thawed on ice on the day of experiment.

Cell culture and transfection

The HEK293 cell line subclone TS201A was a gift from Vladimir Yarov-Yarovoy and was maintained in Dulbecco's modified Eagle's medium (Gibco, Waltham, MA, 11995-065) with 10% fetal bovine serum (HyClone, Logan, UT, SH30071.03HI, LotAXM55317) and 1% penicillin/streptomycin (Gibco, 15-140-122) in a humidified incubator at 37°C under 5% CO₂. Chinese hamster ovary (CHO) cell lines were a tetracycline-regulated expression variant (Invitrogen, Waltham, MA, R71807) and were cultured as described previously (47). The Kv2.1-CHO cell subclone (49) was stably transfected with pCDNA4/TO encoding the rat Kv2.1 (rKv2.1) channel. Cell lines were negative for mycoplasma based on a biochemical test (Lonza, Basel, Switzerland, LT07). 1 μ g/mL minocycline (Enzo Life Sciences, Farmingdale, NY), prepared in 70% ethanol, was added to Kv2.1-CHO cells to induce rKv2.1 channel expression for 1.5 h to minimize series-resistance-induced voltage errors in K⁺-current recordings or for 48 h to produce sufficient Kv2.1 density necessary for recording gating currents. 5 min prior to transfection, cells were plated at 40% confluency in un-supplemented culture media free of antibiotics, selection agents, and serum and allowed to settle at room temperature. For imaging studies (except concentration-response), cells were plated in 35 mm no. 1.5 glass-bottom dishes (MatTek, Ashland, MA, P35G-1.5-20-C). For concentration-response time-lapse imaging, cells were plated onto 22 \times 22 mm no. 1.5H cover glass (Deckglaser). For electrophysiological studies, cells were plated in 35 mm tissue-culture-treated polystyrene dishes (Thermo Fisher Scientific, Waltham, MA, 12-556-000). Transfections were achieved with Lipofectamine 2000 (Life Technologies, Carlsbad, CA, 11668-027). Each transfection included 220 μ L Opti-MEM (Life Technologies, 31985062), 1.1 μ L Lipofectamine, and the specified amount of plasmid DNA. HEK293 cell experiments included 0.1 μ g of mKv2.1 DNA and either 0.1 μ g plasmid encoding enhanced green fluorescent protein (pEGFP), mAMIGO1-pIRES2-GFP DNA, or hSCN1 β -pIRES2-GFP. The pIRES2-GFP vector has an encoded internal ribosome entry site that promotes continuous translation of two genes from a singular mRNA (50) so that GFP fluorescence indicates the presence of AMIGO1 or SCN1 β mRNA. Kv2.1-CHO cell experiments included 1 μ g of either mAMIGO1-pEYFP-N1, pEGFP, rAMIGO2-pEYFP-N1, or rAMIGO3-pEYFP-N1. CHO cell experiments included 1 μ g of both pCAG-Chrome-mRuby2-ST and mAMIGO1-pEYFP-N1. Cells were incubated in the transfection cocktail and 2 mL of un-supplemented media for 6–8 h before being returned to regular growth media and were used for

experiments 40–48 h after transfection. pEGFP, mAMIGO1-pEYFP-N1, and pCAG-ChroME-mRuby2-ST (51) plasmids were gifts from James Trimmer. mAMIGO1-pEYFP-N1 uses a VPRARDPPVAT linker to tag the internal C-terminus of wild-type mouse AMIGO1 (NM_001004293.2 or NM_146137.3) with enhanced yellow fluorescent protein (eYFP). pCAG-ChroME-mRuby2-ST encodes an mRuby2-tagged channelrhodopsin with a Kv2.1 PRC trafficking sequence (51,52). mKv2.1 (NM_008420) was purchased from OriGene (Rockville, MD, MG210968). hSCN1 β -pIRES2-GFP was a gift from Vladimir Yarov-Yarovoy. mAMIGO1 was subcloned into pIRES2-GFP between NheI and BamHI restriction sites. rAMIGO2-pEYFP-N1 and rAMIGO3-pEYFP-N1 were generated by subcloning rat AMIGO2 (NM_182816.2) or rat AMIGO3 (NM_178144.1) in place of mAMIGO1 in the mAMIGO1-pEYFP-N1 vector.

Whole-cell K⁺ ionic currents

Voltage clamp was achieved with an Axopatch 200B patch-clamp amplifier (Molecular Devices, San Jose, CA, USA) run by Patchmaster (HEKA, Lambrecht, Germany). Solutions included HEK293 internal (in mM) 160 KCl, 5 EGTA, 10 HEPES, 1 CaCl₂, 2 MgCl₂, and 10 glucose, adjusted to pH 7.3 with KOH, 345 mOsm; HEK293 external (in mM) 5 KCl, 160 NaCl, 10 HEPES, 2 CaCl₂, 2 MgCl₂, 10 glucose, adjusted to pH 7.3 with NaOH, 345 mOsm, and 5 μ M tetrodotoxin was added to the recording solution: liquid junction potential (LJP) was 3.9 mV and E_K was -89.0 mV with HEK293 internal; Kv2.1-CHO internal (in mM) 70 KCl, 5 EGTA, 50 HEPES, 50 KF, and 35 KOH, adjusted to pH 7.4 with KOH, 310 mOsm; Kv2.1-CHO external (in mM) 3.5 KCl, 155 NaCl, 10 HEPES, 1.5 CaCl₂, 1 MgCl₂, adjusted to pH 7.4 with NaOH, 315 mOsm; LJP was 8.5 mV and E_K was -97.4 mV with Kv2.1-CHO cell internal; high Mg²⁺ Kv2.1-CHO external (in mM) 3.5 KCl, 6.5 NaCl, 10 HEPES, 1.5 CaCl₂, 100 MgCl₂, adjusted to pH 7.4 with NaOH, 289 mOsm; LJP was 13.1 mV and E_K was -97.4 mV with Kv2.1-CHO internal. Osmolality was measured with a vapor pressure osmometer (Wescor, Logan, UT, 5520), and a 5% difference between batches was tolerated. LJP values were tabulated using Patcher's Power Tools version 2.15 (Max-Planck, Munich, Germany), and corrected post hoc during analysis. Voltage protocols list command voltages prior to LJP correction. Kv2.1CHO cells were harvested by scraping in Versene (Gibco, 15040066) or TrypLE (Gibco, 12563011). HEK293 cells were dislodged by scraping. Cells were washed three times in a polypropylene tube in the external solution used in the recording chamber bath by pelleting at 1000 \times g for 2 min and rotated at room temperature (22–24°C) until use. Cells were then pipetted into a 50 μ L recording chamber (Warner Instruments, Hamden, CT, RC-24N) and allowed to settle for 5 or more minutes. After adhering to the bottom of the glass recording chamber, cells were rinsed with external solution using a gravity-driven perfusion system. Cells showing plasma-membrane-associated YFP, or intracellular GFP of intermediate intensity, were selected for patching. Thin-wall borosilicate glass recording pipettes (Sutter, Novato, CA, BF150-110-7.5HP) were pulled with blunt tips, coated with silicone elastomer (Dow Corning, Midland, MI, Sylgard 184), heat cured, and tip fire-polished to resistances less than 4 M Ω . A series resistance of 3–9 M Ω was estimated from the whole-cell parameters circuit. Series resistance compensation (of <90%) was used as needed to constrain voltage errors to less than 10 mV, and the lag was 10 μ s. Cell capacitances were 4–15 pF. Capacitance and Ohmic leak were subtracted using a P/5 protocol. Output was low-pass filtered at 10 kHz using the amplifier's built-in Bessel and digitized at 100 kHz. Traces were filtered at 2 kHz for presentation. The intersweep interval was 2 s. HEK293 cells with less than 65 pA/pF current at +85 mV were excluded to minimize the impact of endogenous K⁺ currents (53). The average current in the final 100 ms at holding potential prior to the voltage step was used to zero subtract each recording. Mean outward current ($I_{avg,step}$) was an amplitude between 90 and 100 ms post depolarization. Mean tail current was the current amplitude between 0.2 and 1.2 ms into the 0 mV step. 100 μ L of 100 nM GxTX-594 was flowed over cells

with a membrane resistance greater than 1 G Ω , pulses to 0 mV were gauged over the time course of binding, and the G - V protocol was run. Data with a predicted voltage error $V_{error} \geq 10$ mV was excluded from analysis. V_{error} was tabulated using estimated series resistance post compensation ($R_{s,post}$):

$$V_{error} = I_{avg,step} * R_{s,post}. \quad (1)$$

For G - V profiles, the cell membrane voltage ($V_{membrane}$) was adjusted by V_{error} and LJP :

$$V_{membrane} = V_{command} - V_{error} - LJP. \quad (2)$$

Tail currents were normalized by the mean current from 50 to 80 mV. Fitting was carried out using Igor Pro software, version 7 or 8 (Wavemetrics, Lake Oswego, OR) that employs nonlinear least squares curve fitting via the Levenberg-Marquardt algorithm. To represent the four independent and identical voltage sensors that must all activate for channels to open, G - V relations were individually fit with a fourth power Boltzmann:

$$f(V) = A \left(1 + e^{\frac{-(V-V_{1/2})zF}{RT}} \right)^{-x}, \quad (3)$$

where $f(V)$ is normalized conductance (G), A is maximum amplitude, x is the number of independent identical transitions required to reach full conductance (for a fourth power function, $x = 4$), $V_{1/2}$ is activation midpoint, z is the valence in units of elementary charge (e_0), F is the Faraday constant, R is the ideal gas constant, and T is absolute temperature. The half-maximal voltage (V_{Mid}) for fourth-power functions is

$$V_{Mid} = V_{i,1/2} + \frac{42.38}{z_i}. \quad (4)$$

Reconstructed Boltzmann curves use average z_i and $V_{1/2} \pm$ SD. The minimum Gibbs free energy (ΔG_{AMIGO1}) that AMIGO1 imparts to conductance, was tabulated as

$$\Delta G = -R \times T \times \ln(K_{eq}). \quad (5)$$

Here, $R = 0.00199$ kcal/(K \cdot mol), and $T = 298$ K. K_{eq} , or the equilibrium constant of channel opening, was approximated by $\frac{f_{Kv2.1+AMIGO1}(V_{i,Mid,Kv2.1})}{1-f_{Kv2.1+AMIGO1}(V_{i,Mid,Kv2.1})}$ where $f_{Kv2.1+AMIGO1}(V_{i,Mid,Kv2.1})$ is the reconstructed relative conductance of Kv2.1 + AMIGO1 at $V_{i,Mid}$ of Kv2.1-control cells (Table 1).

Activation time constants (τ_{act}) and sigmoidicity values (σ) (54) were derived by fitting 10–90% current rise with

$$I_K = A \left(1 - e^{-\frac{t}{\tau_{act}}} \right)^\sigma, \quad (6)$$

where current at end of step, $I_{avg,step}$, was set to 100%. $t = 0$ was adjusted to 100 μ s after the voltage step start to correct for filter delay and cell charging. Deactivation time constants (τ_{deact}) were from fitting 1 to 100 ms of the current decay during 0 mV tail step with an exponential function

$$I_K = y_0 + Ae^{-\frac{t-t_0}{\tau_{deact}}}. \quad (7)$$

Reported τ_{deact} was the average after steps to +10 to +120 mV or +50 to +120 mV in GxTX-594. Kv2.1 deactivation kinetics became progressively slower after the establishment of the whole-cell mode, similar to Shaker deactivation after patch excision (55). Due to the increased variability of deactivation kinetics expected from this slowing phenomenon, deactivation kinetics were not analyzed further.

TABLE 1 Fourth-order Boltzmann parameters for G - V relationships

	G - V fit parameters				ΔG_{AMIGO1} (kcal/mol) (Eq. 5)
	$V_{i,1/2}$ (mV)	$V_{i,Mid}$ (mV)	z_i (e_0)	n	
HEK293 cells					
mKv2.1 + GFP	-26.8 ± 3.0	1.7 ± 1.4^A	1.79 ± 0.17^D	7	-0.31
mKv2.1 + AMIGO1 + GFP	-30.9 ± 0.8	-7.4 ± 1.8^B	1.95 ± 0.16^E	14	
mKv2.1 + SCN β 1 + GFP	-24.8 ± 1.5	0.2 ± 1.8^C	1.720 ± 0.074^F	8	
Kv2.1-CHO cells					
rKv2.1 + GFP	-33.4 ± 1.7	-1.8 ± 1.2^G	1.411 ± 0.070^I	20	-0.28
rKv2.1 + AMIGO1-YFP	-42.0 ± 3.3	-7.6 ± 1.8^H	1.40 ± 0.11^J	19	
Kv2.1-CHO cells + Mg^{2+}					
rKv2.1 + GFP	-13.8 ± 1.8	17.6 ± 2.2^K	1.51 ± 0.11^M	18	-0.37
rKv2.1 + AMIGO1-YFP	-16.3 ± 1.5	10.2 ± 1.0^L	1.682 ± 0.082^N	23	
Kv2.1-CHO cells + GxTX-594					
rKv2.1 + GFP	26.8 ± 2.9	73.2 ± 3.8^O	1.03 ± 0.11^Q	13	-0.77
rKv2.1 + AMIGO1-YFP	12.9 ± 4.4	50.9 ± 2.8^P	1.27 ± 0.14^R	12	

Average $V_{i,1/2}$, $V_{i,Mid}$, and z_i values were derived from a fourth-order Boltzmann fits (Eq. 3) of n individual cells. All values are given means \pm SEM. Brown-Forsythe and Welch (appropriate for differing SD) analysis of variance test with Dunnett's T3 multiple comparisons p values: AB: 0.046. AC: 0.64. DE: 0.75. DF: 0.91. Unpaired, two-tailed t -test p values: GH: 0.012. IJ: 0.95. KL: 0.0051. MN: 0.21. OP: 0.00018. QR: 0.19. ΔG_{AMIGO1} from Eq. 5, at $V_{i,Mid}$ for Kv2.1 + GFP.

On-cell single-channel K^+ currents

Single-channel recordings were made from on-cell patches to avoid the Kv2.1 current rundown that occurs after patch excision (56). Methods same as whole-cell K^+ ionic currents were used unless otherwise noted. While cells selected for recording had AMIGO1-YFP fluorescence apparent at the surface membrane, we cannot be certain each single Kv2.1 channel interacted with AMIGO1. Solutions included Kv2.1-CHO single-channel internal (in mM) 155 NaCl, 50 HEPES, 20 KOH, 2 CaCl₂, 2 MgCl₂, 0.1 EDTA, adjusted to pH 7.3 with HCl, 347 mOsm; and Kv2.1-CHO single channel external (in mM) 135 KCl, 50 HEPES, 20 KOH, 20 NaOH, 2 CaCl₂, 2 MgCl₂, 0.1 EDTA, adjusted to pH 7.3 with HCl, 346 mOsm: LJP -3.3 mV with Kv2.1-CHO single-channel internal. Thick-wall borosilicate glass (BF150-86-7.5HP, Sutter Instruments) was pulled, Sylgard coated and fire polished, to resistances >10 M Ω . Analysis methods were the same as those previously used (5) unless noted. To subtract capacitive transients, traces without openings were averaged and subtracted from each trace with single-channel openings. Peaks in single-channel amplitude histograms were fit to half maximum with a Gaussian function to define the single-channel opening level for idealization by a half-amplitude threshold. Open dwell times were well described by a single exponential component that was used to derive $\tau_{closing}$. Average open dwell times were also described as the geometric mean of all open dwell times. Closed dwell times appeared to have multiple exponential components and were solely described as the geometric mean of all closed dwell times.

Whole-cell gating-current measurements

Methods were the same as those used for whole-cell K^+ ionic currents unless noted. Solutions included gating-current internal (in mM) 90 NMDG, 1 NMDG-Cl, 50 HEPES, 5 EGTA, 50 NMDG-F, 0.01 CsCl, adjusted to pH 7.4 with methanesulfonic acid, 303 mOsm; and gating-current external (in mM) 150 TEA-Cl, 41 HEPES, 1 MgCl₂ · 6 H₂O, 1.5 CaCl₂, adjusted to pH to 7.3 with NMDG, 311 mOsm: LJP -3.3 mV with gating-current internal. To avoid KCl contamination of the recording solution from the pH electrode, pH was determined in small aliquots that were discarded. Cells were resuspended in Kv2.1-CHO external and washed in the recording chamber with 10 mL gating-current external.

Pipettes has resistances of 6–14 M Ω . Series resistances were 14–30 M Ω and were compensated 50%. Cell capacitances were 6–10 pF. V_{error} was negligible (<1 mV). P/5.9 leak pulses were from a -133 mV leak holding potential. An early component ON-gating-charge movement was quantified by integrating ON gating currents in a 3.5-ms window ($Q_{ON,fast}$) following the end of fast capacitive artifacts created from the test voltage step (which usually concluded 0.1 ms following the voltage step). The slow tail of the ON-charge movement is difficult to accurately integrate in these cells, making the cutoff point arbitrary. This 3.5-ms integration window resulted in a more positive $Q_{ON,fast}$ - V midpoint than with a 10-ms window (5) and a more positive midpoint than the G - V relation. Differences in gating-current solutions compared with prior studies may also contribute to the different midpoints reported (4,5,57). Currents were baseline subtracted from 4 to 5 ms into the step. Q_{OFF} was determined by integration of OFF-charge movement in a 9.95-ms window after capacitive artifacts (usually 0.1 ms). Currents were baseline subtracted from 10 to 20 ms into the step. Gating-charge density fC/pF was normalized by cell capacitance. Q - V curves were normalized to an average of 100–120 mV. Q - V relations were individually fit with a first-power Boltzmann (Eq. 3, $x = 1$). Time constants (τ_{ON}) were determined from a double-exponential fit function:

$$I_{g,ON} = A \left(e^{-\frac{t}{\tau_{ON}}} \right) + B - A_{rise} \left(e^{-\frac{t}{\tau_{rise}}} \right). \quad (8)$$

τ_{rise} was not used in analyses. $I_{g,OFF}$ was not well fit by Eq. 8, and τ_{OFF} was not analyzed. The voltage dependence of the forward voltage-sensor-activation (α) rate was determined by fitting the average τ_{ON} - V weighted by the standard error:

$$\tau_{ON} = \frac{1}{\alpha_{0mV} e^{V_{z\alpha F}/RT} + \beta_{0mV} e^{V_{z\beta F}/RT}}. \quad (9)$$

Reverse rates were not analyzed. The energy of AMIGO1's impact on the activation rate of all four voltage sensors ($\Delta G_{AMIGO1}^\ddagger$) was

$$\Delta G = -4 \times R \times T \times \ln \left(\frac{k_{Kv2.1+AMIGO1}}{k_{Kv2.1}} \right), \quad (10)$$

where $k = \alpha_{0mV}$. Estimates of ΔG_{AMIGO1} from Q - V relations were with Eq. 5 or

$$\Delta G = V_{1/2} \times Q \times F. \quad (11)$$

Here, $F = 23.06 \text{ kcal/V} \cdot \text{mol} \cdot e_0$. Q was either z_g from fits or $12.5 e_0$ as determined from a limiting slope analysis of the Kv2.1 open probability-voltage relation (3). $V_{1/2}$ was either $V_{g,Mid}$ or a median voltage ($V_{g,Med}$) as calculated from integration above and below Q_{OFF} - V relations using a trapezoidal rule (58).

Fluorescence imaging

Images were obtained with an inverted confocal/airy disk imaging system with a diffraction grating separating 400–700 nm emission into 9.6 nm bins (Zeiss, Jena, Germany, LSM 880, 410900-247-075) run by ZEN black version 2.1. Laser lines were 3.2 mW (488 nm), 1.2 mW (514 nm), 0.36 mW (543 nm), and 0.60 mW (594 nm). Images were acquired with a 1.4 numerical aperture (NA) 63x (Zeiss 420782-9900-799), 1.3 NA 40x (Zeiss 420462-9900-000), or 1.15 NA 63x objectives (Zeiss 421887-9970-000). Images were taken in either confocal or airy disk imaging mode. The imaging solution was Kv2.1-CHO external supplemented with 0.1% bovine serum albumin and 10 mM glucose. The temperature inside the microscope housing was 24–28°C. Representative images had brightness and contrast adjusted linearly.

Concentration-effect imaging

Cells plated on coverslips were washed 3 times with imaging solution and then mounted on an imaging chamber (Warner Instruments, RC-24E) with vacuum grease. 100 μL GxTX-594 dilutions were applied for 10 min then washed out by flushing 10 mL at a flow rate of $\sim 1 \text{ mL}/10 \text{ s}$. 15 min after wash out, the next GxTX-594 concentration was added. Airy disk imaging had a 1.4 NA 63x objective (Zeiss 420782-9900-799), 0.13 μm pixels, 0.85 μs dwell, and a 5-s frame rate. YFP excitation had 488 nm 2% power and an emission of 495–550 nm. GxTX-594 excitation had 594 nm 2% power and an emission of 495–620 nm. Intensities were extracted using FIJI (59). Regions of interest were drawn around groups of cells \pm YFP fluorescence. Dissociation constant (K_d) fit with fluorescence intensity at 0 nM GxTX-594 was set to 0 with

$$f(x) = A \frac{1}{(1 + K_d/x)} + B. \quad (12)$$

Voltage clamp fluorimetry was conducted as described (45). Briefly, 100 μL 100 nM GxTX-594 in imaging external was applied for 10 min then diluted with 1 mL Kv2.1-CHO external for imaging. Airy disk imaging had a 1.15 NA 63x objective (Zeiss 421887-9970-000), 0.11 μm pixels, 0.85 μs dwell, 2x averaging, and a 1-s frame rate. GxTX-594 excitation had 594 nm 1% power and an emission of 605 nm longpass. Cells with obvious GxTX-594 labeling were whole-cell voltage clamped. Voltage-clamp fluorimetry internal included (in mM) 70 mM CsCl, 50 mM CsF, 35mM NaCl, 1 mM EGTA, 10 mM HEPES, adjusted to pH 7.4 with CsOH, 310 mOsm: LJP -5.3 mV with Kv2.1-CHO external. Pipettes from thin-wall glass were less than 3.0 M Ω . Cells were held at -100 mV for 30 images and stepped up to +35 mV until fluorescence changes appeared complete. Intensity data were extracted using Zen Blue from regions of interest drawn around an apparent surface-membrane-excluding pipette region. For presentation, fluorescence-intensity traces were normalized from minimum to maximum. The rate of GxTX-594 dissociation (k_{dF}) was fit with a monoexponential function (Eq. 7), and the K_{eq} for resting versus activated voltage sensors was calculated as described (45). ΔG_{AMIGO1} was from Eq. 11, where $k = K_{eq}$.

Environment-sensitive fluorescence imaging was done with GxTX Ser13Pra(JP) and GxTX Lys27Pra(JP). Cells were incubated in 100 μL GxTX(JP) solution for 5–10 min then washed with imaging solution. Spectral confocal imaging had a 1.4 NA 63x objective, 0.24 μm pixels,

8.24 μs dwell, 2x averaging. YFP excitation was 514 nm. GxTX Ser13Pra(JP) excitation was 594 nm. GxTX Lys27Pra(JP) excitation was 543 nm. Fluorescence counts were extracted in Zen Blue. JP emission spectra were fit with two-component split pseudo-Voigt functions (46) using the curve-fitting software Fityk 1.3.1 (<https://fityk.nieto.pl/>), which employed a Levenberg-Marquardt algorithm. Goodness of fit was determined by root-mean-squared deviation values, which are listed in Table S2 along with the parameters of each component function. To avoid YFP overlap, fittings for spectra from cells expressing AMIGO1-YFP include emission data points from 613–700 nm for GxTX Ser13Pra(JP) and 582–700 nm for GxTX Lys27Pra(JP). Fittings for JP spectra from cells without AMIGO1-YFP included all data from 550–700 nm.

Experimental design and statistical treatment

Independent replicates (n) are individual cells pooled over multiple transfections. The n values from each transfection for each figure are listed in Tables S3 and S4. In each figure panel, control and test cells were plated side by side from the same suspensions and transfected side by side, and the data were acquired from control and test cells in an interleaved fashion. Identity of transfected constructs was blinded during analysis. Analysis of variance of transfection- or acquisition-date-dependent variance of Boltzmann fit parameters and Pearson's correlation coefficient (PCC)/coefficient of variation (COV) did not reveal a dependence, and all n values were pooled. Statistical tests were conducted with Prism 9 (GraphPad Software, San Diego, CA), and details are included in the figure legends.

RESULTS

AMIGO1 shifts the midpoint for activation of Kv2.1 conductance

Voltage-clamp recordings from co-transfected HEK293 cells indicate that mouse AMIGO1 shifts the G - V relation of mouse Kv2.1 by $-5.7 \pm 2.3 \text{ mV}$ (standard error of the mean [SEM]) (Fig. S1). This shift was similar to the $-6.1 \pm 1.6 \text{ mV}$ shift reported for rat Kv2.1-GFP by human AMIGO1-mRuby2 (23) and smaller than the -15.3 mV (no error listed) shift of mouse Kv2.1-GFP by mouse AMIGO1 (22). This small effect of AMIGO1 was similar to the cell-to-cell variability in our recordings. We suspected that endogenous voltage-activated conductances of HEK293 cells (53,60) and the variability inherent to transient co-transfection could increase variability. To minimize possible sources of cell-to-cell variability, further experiments were with a CHO K1 cell line with inducible rat Kv2.1 expression (Kv2.1-CHO) transfected with a YFP-tagged mouse AMIGO1. Inducible Kv2.1 expression permits tighter control of current density (49), and fluorescence tagging of AMIGO1 permits visualization of protein expression and localization. Unlike HEK293 cells, CHO cells lack endogenous voltage-gated K^+ currents (61).

As expression systems can influence auxiliary protein interactions with ion channels (62–66), we assessed Kv2.1-AMIGO1 association in these CHO cells. We evaluated two hallmarks of Kv2.1 and AMIGO1 association: Kv2.1 reorganization of AMIGO1, and AMIGO1/Kv2.1 co-localization (22,23,28).

In HEK293 cells, heterologously expressed AMIGO1 localization is intracellular and diffuse (23,28). However, when co-expressed with Kv2.1, AMIGO1 reorganizes into puncta with Kv2.1, similar to the expression patterns in central neurons (23,28). To determine whether Kv2.1 reorganizes AMIGO1 in Kv2.1-CHO cells, the degree of AMIGO1-YFP reorganization was quantified using the COV, which captures non-uniformity of YFP localization (67). COV was quantified following the limited 1.5-h Kv2.1 induction period used in whole-cell and single-channel K^+ -current recordings and the prolonged 48-h induction period used for gating-current recordings or imaging studies. COVs were compared against an uninduced control (0-h induction) and against an engineered protein, ChroME-mRuby2, which contains the Kv2.1 PRC trafficking sequence but lacks the Kv2.1 voltage-sensing and pore-forming domains (51,52). COVs were evaluated from the glass-adhered basal membrane where evidence of reorganization is most notable (Fig. 1). Both $COV_{1.5h}$ and COV_{48h} were greater than the COV_{0h} or $COV_{ChroME-mRuby2}$ control. This result is consistent with Kv2.1 and AMIGO1 association in CHO cells.

As an additional measure of whether Kv2.1 reorganizes AMIGO1 in Kv2.1-CHO cells, we assessed AMIGO1-YFP and Kv2.1 co-localization using the PCC (68). Surface-expressing Kv2.1 on live cells was labeled with GxTX Ser13Cys(Alexa594), a conjugate of a voltage-sensor toxin guangxitoxin-1E derivative with a fluorophore, abbreviated

GxTX-594 (45). As auxiliary subunits can impede binding of toxins to voltage-gated ion channels (69), we tested whether AMIGO1 impacted GxTX-594 binding to Kv2.1. Under conditions with prolonged Kv2.1 induction, where AMIGO1 modulates most, if not all, Kv2.1 voltage-sensor movements, we found no evidence that AMIGO1 impedes GxTX-594 binding to Kv2.1 (Fig. S2). Co-localization between AMIGO1-YFP and GxTX-594 was apparent as PCC_{48h} , measured from the glass-adhered basal membrane, was greater than the negative control, $PCC_{ChroME-mRuby2}$ (Fig. 2 B). With a limited 1.5-h induction, GxTX-594 was difficult to detect at the glass-adhered membrane, so we moved the confocal imaging plane further from the cover glass to image Kv2.1 on apical cell surfaces where GxTX-594 labeling was more apparent. On these apical surfaces, $PCC_{1.5h}$ and PCC_{48h} were greater than PCC_{0h} (Fig. 2 A), consistent with some co-localization of AMIGO1-YFP and Kv2.1. The weakly significant increase of the $PCC_{1.5h}$ compared with PCC_{0h} is consistent with some co-localization. Disproportionate expression can skew PCC values (70), and the limited GxTX-594 signal was expected to depress the $PCC_{1.5h}$ value. Similarly, the lower PCC_{48h} values were associated with either minimal or exceptionally bright AMIGO1-YFP signals. Overall, we saw no sign of Kv2.1 channels lacking co-localized AMIGO1 in cells with high levels of AMIGO1 expression. Altogether, the reorganization and co-localization indicate that AMIGO1-YFP and Kv2.1 interact in the CHO cells

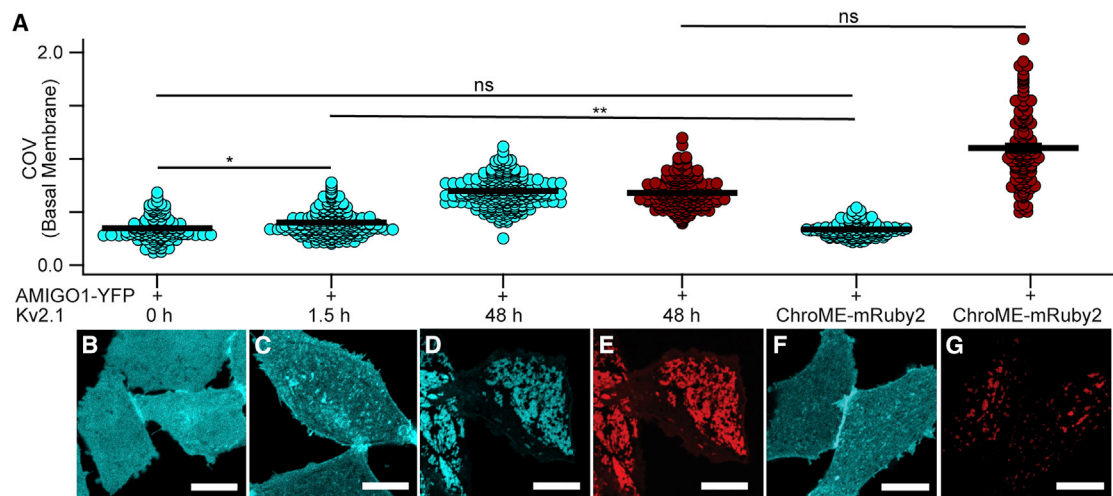


FIGURE 1 Kv2.1 reorganizes AMIGO1 in CHO cells. (A) Coefficient of variation of fluorescence from AMIGO1-YFP (blue circles), GxTX-594 (red circles), or ChroME-mRuby2 (red circles). Bars are mean \pm SEM. COV measurements were calculated from confocal images acquired from the glass-adhered basal membrane of the cell (exemplar confocal images in B–G). All cells were transfected with AMIGO1-YFP 48 h prior to imaging. COV from individual cells (n) were pooled from 4 separate transfections for each experimental condition. AMIGO1-YFP fluorescence from cells (B) not induced for Kv2.1 expression ($COV_{0h} = 0.3492 \pm 0.0098$, $n = 134$), (C) induced 1.5 h ($COV_{1.5h} = 0.4013 \pm 0.0077$, $n = 217$), and (D) induced 48 h ($COV_{48h} = 0.6984 \pm 0.0083$, $n = 277$). (E) GxTX-594 labeling from (D) ($COV_{48h(GxTX-594)} = 0.6822 \pm 0.010$, $n = 197$). (F) AMIGO1-YFP fluorescence from CHO cells that lack Kv2.1 co-transfected with ChroME-mRuby2 ($COV_{lack} = 0.3377 \pm 0.0059$, $n = 125$). (G) ChroME-mRuby2 fluorescence from (F) ($COV_{ChroME-mRuby2} = 1.102 \pm 0.030$, $n = 128$). Scale bars, 10 μ m. (Statistics) Outliers removed using ROUT, $Q = 1\%$. Ordinary one-way analysis of variance with multiple comparisons. p values: $COV_{0h}COV_{1.5h}$: $p = 0.0467$; $COV_{0h}COV_{lack}$: $p = 0.9936$; $COV_{1.5h}COV_{lack}$: $p = 0.0081$; $COV_{48h(GxTX-594)}COV_{(ChroME-mRuby2)}$: $p = 0.9010$. All other p values were ≤ 0.0001 . To see this figure in color, go online.

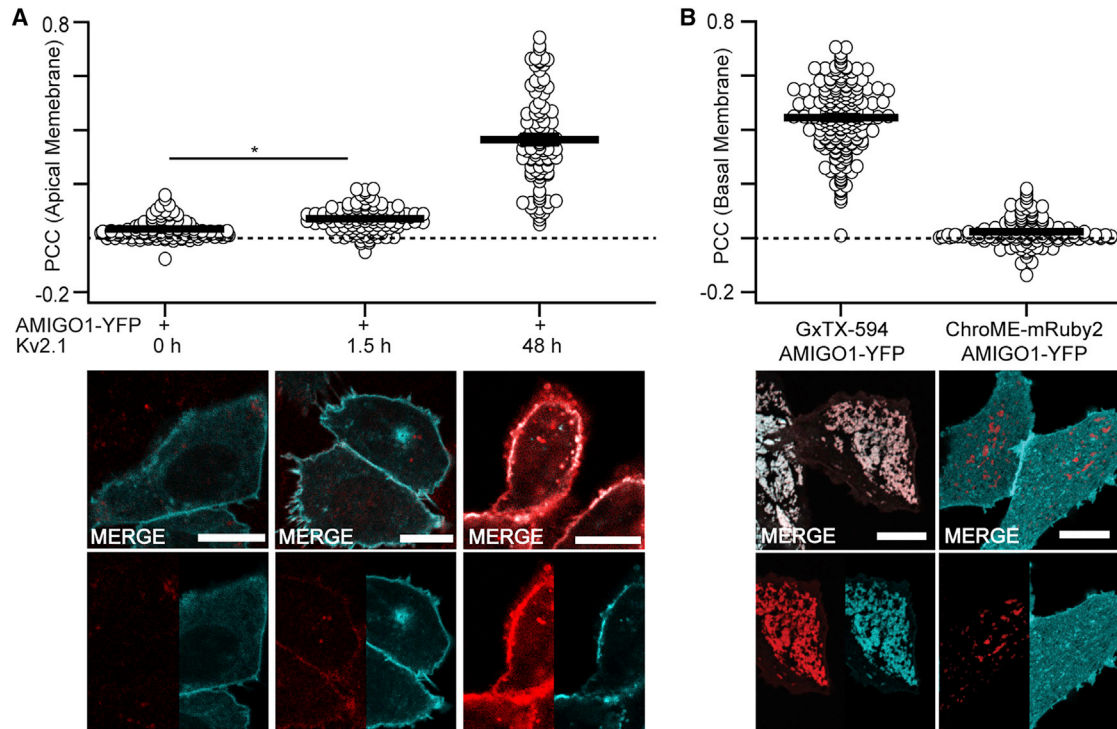


FIGURE 2 AMIGO1 colocalizes with Kv2.1 in CHO cells. (A) Costes thresholded, Pearson's co-localization between AMIGO1-YFP and GxTX-594 at cell membrane following, from left to right, 0, 1.5, or 48 h of Kv2.1 induction (exemplar confocal images in *B–J* below). Mean \pm SEM (one-tailed ≥ 0 t-test): $PCC_{0h} = 0.0321 \pm 0.0033$ ($p < 0.0001$), $n = 101$; $PCC_{1.5h} = 0.0718 \pm 0.0042$ ($p < 0.0001$), $n = 118$; and $PCC_{48h} = 0.365 \pm 0.017$ ($p < 0.0001$), $n = 101$. (B) Costes thresholded, Pearson's co-localization between (left to right) AMIGO1-YFP/GxTX-594 and AMIGO1-YFP/ChroME-mRuby2 at the glass-adhered basal membrane of the cell. Exemplar images are the same as in *Fig. 1 D–G*. From left to right: $PCC_{GxTX-594} = 0.4449 \pm 0.0090$ ($p < 0.0001$), $n = 195$; $PCC_{ChroME-mRuby2} = 0.0242 \pm 0.0045$ ($p < 0.0001$), $n = 129$. Image panels with merge overlays (white) of GxTX-594 (red) and AMIGO1-YFP (cyan) correspond to conditions above. All scale bars, 10 μ m. (Statistics) Outliers were removed using ROUT, $Q = 1\%$. Ordinary one-way analysis of variance with multiple comparisons. p values: $PCC_{0h}PCC_{1.5h}$: $p = 0.346$; $PCC_{1.5h}PCC_{ChroME-mRuby2}$: $p = 0.0025$; $PCC_{0h}PCC_{ChroME-mRuby2}$: $p = 0.9777$. All other p values were ≤ 0.0001 . To see this figure in color, go online.

used for K^+ -current recordings and for gating-current measurements.

AMIGO1 shifts the midpoint of activation of Kv2.1 conductance in CHO cells

To determine whether AMIGO1 affected the macroscopic K^+ conductance in Kv2.1-CHO cells, we conducted whole-cell voltage-clamp recordings. Cells were transfected with GFP (Kv2.1-control cells) or with AMIGO1-YFP (Kv2.1 + AMIGO1 cells) and were identified for the whole-cell voltage clamp based on the presence of cytoplasmic GFP fluorescence or plasma-membrane-associated YFP fluorescence, respectively (*Fig. 3 A*). Macroscopic ionic-current recordings were made in whole-cell voltage-clamp mode, and the K^+ conductance was measured from tail currents (*Fig. 3 B* and *C*). In expectation of small AMIGO1 effects relative to cell-to-cell variation, recordings from control cells and AMIGO1 cells were interleaved during each day of experiments, and cell identity was blinded during analysis. G - V relations were fit with a fourth-power Boltzmann function (*Eq. 3*; *Fig. 3 D, E, and F*), and average midpoints of half-maximal

conduction ($V_{i, Mid}$) and steepness equivalents (z_i) were determined (*Table 1*). In Kv2.1-control cells, the average $V_{i, Mid}$ was -1.8 mV (*Fig. 3 H*), consistent with prior reports of $V_{i, Mid}$ ranging from -3 to $+8$ mV in CHO cells (*4,23,47,71*). Cell-to-cell variation in $V_{i, Mid}$ remained notable between Kv2.1-CHO cells, with variation in $V_{i, Mid}$ on par with other reports (see *Discussion* and *Limitations*). The range of $V_{i, Mid}$ values of Kv2.1 + AMIGO1 cells overlapped with Kv2.1-control cells (*Fig. 3 H*), yet the average $V_{i, Mid}$ was negatively shifted by -5.7 ± 2.2 mV (SE), similar to $\Delta V_{i, Mid}$ from mouse Kv2.1 in HEK293 cells (*Table 1*). No effect on z_i was observed. We also tested AMIGO2 and AMIGO3 on Kv2.1 and found that they co-localize and induce $\Delta V_{i, Mid}$ shifts similar to those reported from HEK293 cells by Maverick and colleagues (*23*) (*Figs. S3 and S4*), indicating that the small G - V shifts by the AMIGO proteins are robust across different experimental preparations.

To test if AMIGO1 also alters the rate of activation of Kv2.1 conductance, we analyzed activation kinetics. The 10–90% of the rise of Kv2.1 currents following a voltage step (*Fig. 3 A* and *B*) was fit with the power of an exponential function (*Eq. 6*) for sigmoidicity (σ), which quantifies

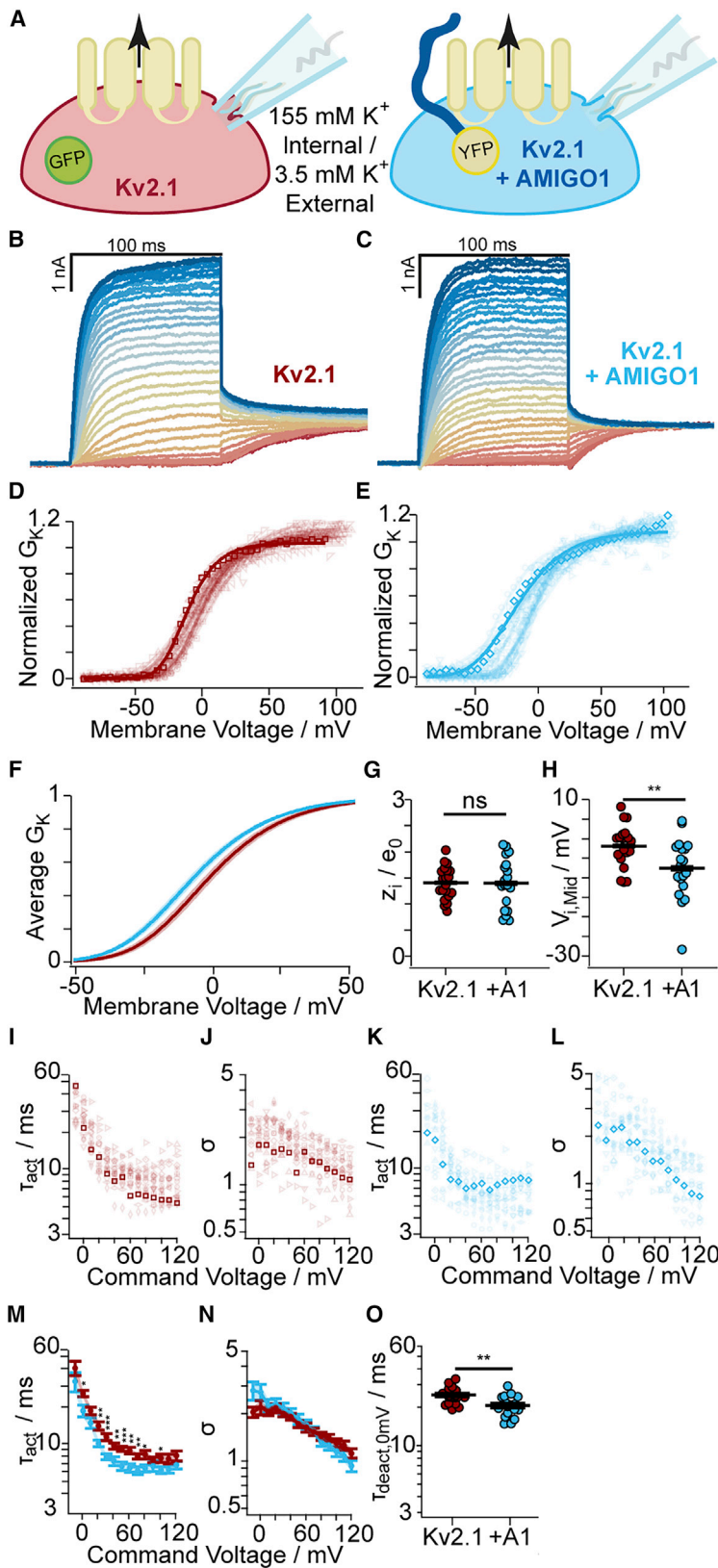


FIGURE 3 AMIGO1 shifts the midpoint and speeds activation of the Kv2.1 conductance in CHO cells. (A) Experimental set up: whole-cell K⁺ currents (arrow) from Kv2.1-CHO transfected with GFP (red) or AMIGO1-YFP (blue). (B and C) Representative Kv2.1-control (6.0 pF) or Kv2.1 + AMIGO1 (14.5 pF) cells. 100-ms voltage steps ranging from -80 (dark red trace) to +120 mV (dark blue trace) in 5-mV increments and then to 0 mV for tail currents. Holding potential was -100 mV. Data points from representative cells are bolded in analysis panels. (D and E) Normalized tail $G-V$ relationships for Kv2.1-control or Kv2.1 + AMIGO1 cells. Symbols correspond to individual cells. Lines are fourth-order Boltzmann fits (Eq. 3). (F) Reconstructed Boltzmann fits from average $V_{i, Mid}$ and z_i (Table 1). Shading $V_{i, Mid} \pm SE$. (G and H) Steepness (G) and midpoint (H) of fits. (I-L) τ_{act} (I and K) and σ (J and L) from fits of Eq. 6 to activation. (M and N) Mean τ_{act} (M) and σ (N). (O) τ_{deact} fits of Eq. 7 to 0 mV tails: Kv2.1-control 24.9 ± 3.6 ms, Kv2.1 + AMIGO1 20.6 ± 3.8 ms. Unpaired t-test $p > 0.5$ between 0 mV τ_{act} and τ_{deact} for Kv2.1-control and Kv2.1 + AMIGO1. All other statistics in Table 1. *** $p = \leq 0.001$, ** $p = \leq 0.01$, * $p = \leq 0.05$, ns, not significant. Bars are mean \pm SEM. To see this figure in color, go online.

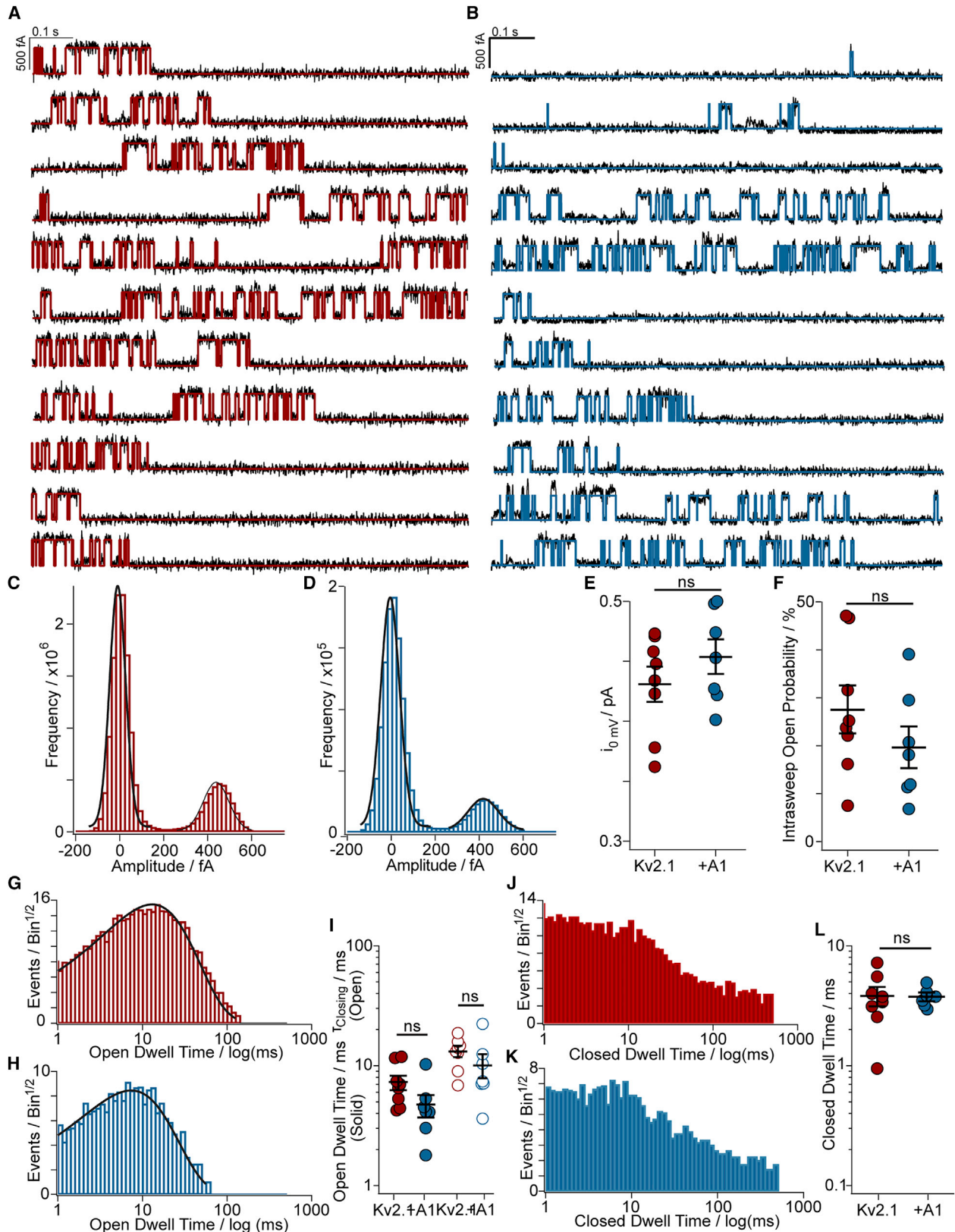


FIGURE 4 Effects of AMIGO1 on pore-opening conformational changes were not apparent in single-channel recordings. (A) Representative single-channel currents at 0 mV from Kv2.1-control and (B) Kv2.1 + AMIGO1. Red or blue lines are idealizations. (C and D) Amplitude histograms at 0 mV from the patches in (A) and (B) fit with Gaussians. (E) Mean single-channel current amplitude: Kv2.1-control 0.43 ± 0.01 pA, Kv2.1 + AMIGO1 0.45 ± 0.02 pA. (F)

(legend continued on next page)

the delay before current rise, and activation time constant (τ_{act}). σ was not significantly altered by AMIGO1 (Fig. 3 *J, L, and N*), suggesting that the Kv2.1 activation pathway retains a similar structure to AMIGO1 (5). At a subset of voltages less than +70 mV, AMIGO1 expression accelerated activation, decreasing τ_{act} (Fig. 3 *I, K, and M*), consistent with results of Maverick and colleagues (23). Following the +10 to +120 mV activating steps, time constants of tail current decay at 0 mV were similar to τ_{act} at 0 mV (Fig. 3 *O, Eq. 7*). A prior study found no impact of AMIGO1 on Kv2.1 deactivation kinetics at -40 mV (23), and deactivation is not studied further here. A model of Kv2.1 activation kinetics suggests that voltage-sensor dynamics influence τ_{act} below $\sim +70$ mV and that at more positive voltages, a slow pore-opening step limits kinetics (5). This analysis suggests that AMIGO1 accelerates activation kinetics only in the voltage range that is sensitive to voltage-sensor dynamics.

Effects of AMIGO1 on pore-opening conformational changes were not apparent in single-channel recordings

To more directly assess whether the pore-opening step of the Kv2.1 activation pathway is modulated by AMIGO1, we analyzed pore openings of single Kv2.1 channels during 1-s-long recordings to 0 mV (Fig. 4 *A and B*). At 0 mV, we expected >85% of all Kv2.1-control voltage sensors or >95% of all Kv2.1-AMIGO1 voltage sensors to activate in less than 2 ms, such that the majority of single-channel openings represent stochastic fluctuations between a closed and open conformation of the pore. Neither the single-channel current amplitude (Fig. 4 *C, D, E*) nor the intrasweep open probability (Fig. 4 *F*) were significantly impacted by AMIGO1. AMIGO1 did not significantly impact the single-channel open or closed dwell times (Fig. 4 *G-L*). These results constrain any impact of AMIGO1 on Kv2.1 pore opening to be smaller than the variability in these single-channel measurements.

A voltage-sensor toxin enhances modulation of AMIGO1 on the Kv2.1 conductance

To test whether AMIGO1 modulation is dependent on voltage-sensor dynamics, we altered voltage-sensor movement with a voltage-sensor toxin. GxTX binds to the voltage-sensing domain of Kv2.1 (72), such that an exit from the earliest resting conformation limits opening to more positive voltages (5). If AMIGO1 modulates voltage

sensors, then GxTX might be expected to amplify the AMIGO1 effect. Alternately, if AMIGO1 acts directly on pore opening, the AMIGO1 impact on the pore-opening equilibrium should persist, regardless of voltage-sensor modulation. To distinguish between these possibilities, we measured AMIGO1 modulation in the presence of the imaging probe GxTX-594, which modulates Kv2.1 by the same mechanism as GxTX (45) and has a similar affinity for the resting conformation of Kv2.1 with or without AMIGO1 (Fig. S2). We applied 100 nM GxTX-594 to cells and activated the Kv2.1 conductance. We note that the 100-ms activating pulses are much shorter than the >2-s time constants of GxTX-594 dissociation at extreme positive voltages (45), and during these short activating pulses, we saw no evidence of GxTX-594 dissociation. The AMIGO1 $\Delta V_{i,\text{Mid}}$ of -22.1 ± 4.8 (SEM) with GxTX-594 was distinct from the AMIGO1 $\Delta V_{i,\text{Mid}}$ of -5.7 ± 2.2 mV (SEM) without GxTX-594 ($p = 0.00018$, unpaired, two-tailed *t*-test), indicating that GxTX-594 amplifies the impact of AMIGO1 on Kv2.1 conductance. We did not observe a significant effect of AMIGO1 on τ_{act} or σ in GxTX-594 (Fig. 5 *J-N*). We calculated the impact of AMIGO1 on a pore-opening equilibrium constant (K_{eq}) at the midpoint of the Kv2.1 *G-V* relation and found a 3.7-fold bias toward a conducting conformation in 100 nM GxTX-594 versus a 1.4-fold bias under control conditions ($\Delta G_{\text{AMIGO1}} = -0.77$ versus -0.28 kcal/mol, respectively; Table 1). This result indicates that the impact AMIGO1 has on the Kv2.1 conductance is dependent on the dynamics of the activation path. Further, this result indicates that AMIGO1 opposes the action of GxTX-594, which stabilizes the earliest resting conformations of the Kv2.1 voltage sensor. We also note that the more dramatic modulation by AMIGO1 with GxTX-594 verifies that most Kv2.1 channels are modulated by AMIGO1 in this cell preparation, in which only a small impact on $V_{i,\text{Mid}}$ was observed without GxTX-594 (Fig. 3).

AMIGO1 facilitates the activation of Kv2.1 voltage sensors

To determine if AMIGO1 affects voltage-sensor movement, we measured gating currents (I_g), which correspond to movement of Kv2.1 voltage sensors across the transmembrane electric field. Kv2.1-CHO cells were patch clamped in whole-cell mode in the absence of K^+ (Fig. 6 *A*) and given voltage steps to elicit gating currents (Fig. 6 *B and C*). The resolvable ON-gating currents ($I_{g,\text{ON}}$) represent an early component of gating-charge movement, but not all

Open probability from amplitude histograms: Kv2.1-control $28 \pm 4.9\%$, Kv2.1 + AMIGO1 $20 \pm 4.2\%$. (*G and H*) Open dwell-time distributions and single exponential fits for a Kv2.1-control (*G*) or Kv2.1 + AMIGO1 (*H*) patch. (*I*) Open dwell times from mean (filled circles) or exponential fit (hollow circles). Kv2.1-control: $13.0 \pm 1.3 \mu\text{s}$; Kv2.1 + AMIGO1: $9.98 \pm 2.3 \mu\text{s}$. (*J and K*) Closed dwell-time distributions and single exponential fit for a Kv2.1-control (*J*) or Kv2.1 + AMIGO1 (*K*) patch. (*L*) Closed dwell times from mean. Kv2.1-control: $3.80 \pm 0.67 \mu\text{s}$; Kv2.1 + AMIGO1: $3.73 \pm 0.250 \mu\text{s}$. ns = two-tailed *t*-test p value > 0.05. Means \pm SEM. To see this figure in color, go online.

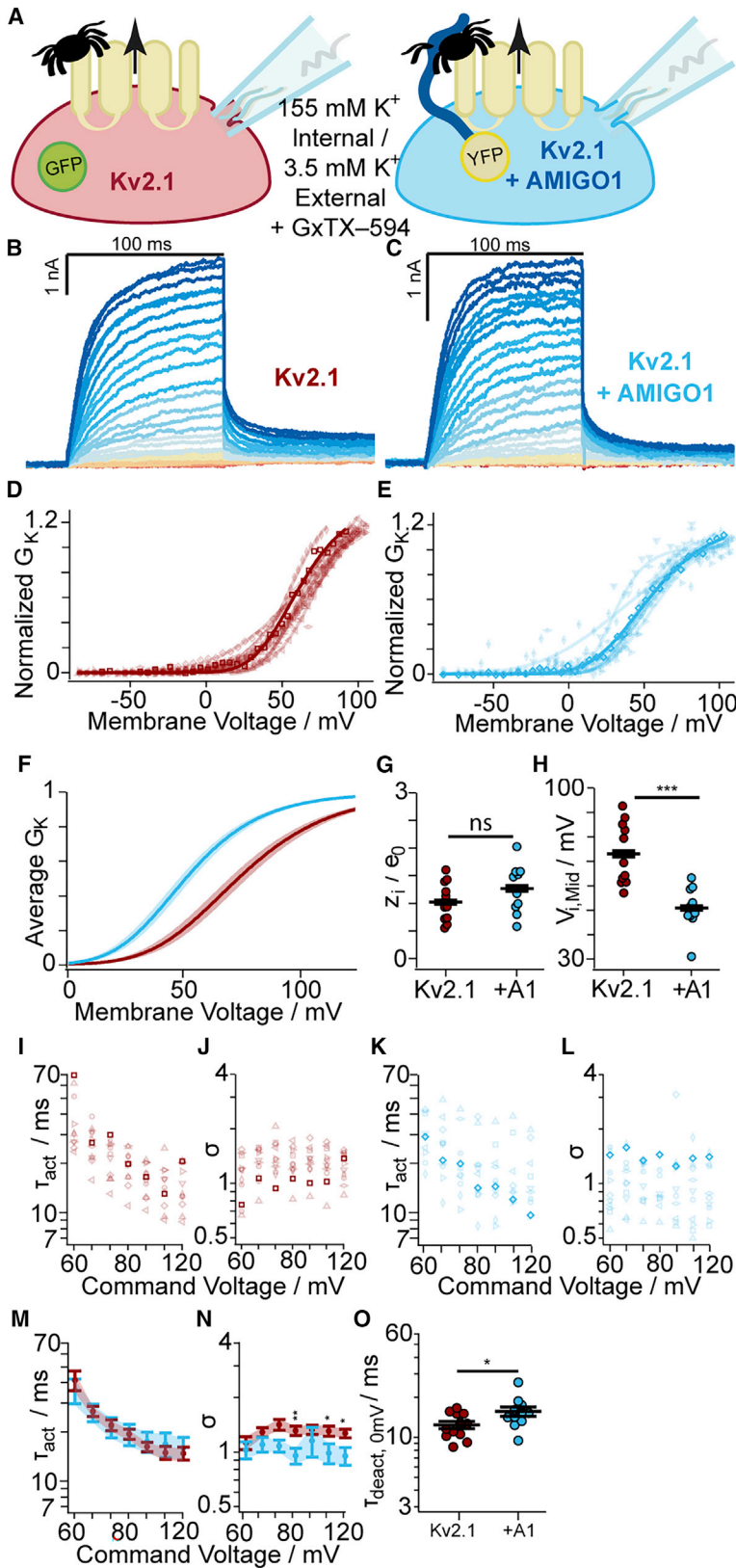


FIGURE 5 The voltage-sensor toxin GxTX-594 enhances AMIGO1 modulation of Kv2.1 conductance. (A) Experimental set up: whole-cell K^+ currents (arrow) from Kv2.1-CHO transfected with GFP (red) or AMIGO1-YFP (blue). Cells were treated with 100 nM GxTX-594 (tarantulas). (B and C) Representative Kv2.1-control (6.0 pF) or Kv2.1 + AMIGO1 (14.5 pF) cells. Same voltage protocol and representations as Fig. 3. (D and E) Normalized G - V relationships. (F) Reconstructed fourth-order Boltzmann fits from $V_{i, Mid}$ and z_i in Table 1. Shading $V_{i, Mid}$ mean \pm SEM. (G and H) Steepness (G) and midpoint (H) of fits. (I-L) τ_{act} (I and K) and σ (J and L) from fits of Eq. 6 to activation. (M and N) Mean τ_{act} (M) and σ (N). (O) τ_{deact} fits of Eq. 7 to 0 mV tails: Kv2.1 with GxTX-594 = 12.4 ± 2.7 ms; Kv2.1 + AMIGO1 with GxTX-594 = 15.7 ± 4.2 ms. All other statistics in Table 1. *** $p \leq 0.001$, ** $p \leq 0.01$, * $p \leq 0.05$, ns, not significant. Bars are mean \pm SEM. To see this figure in color, go online.

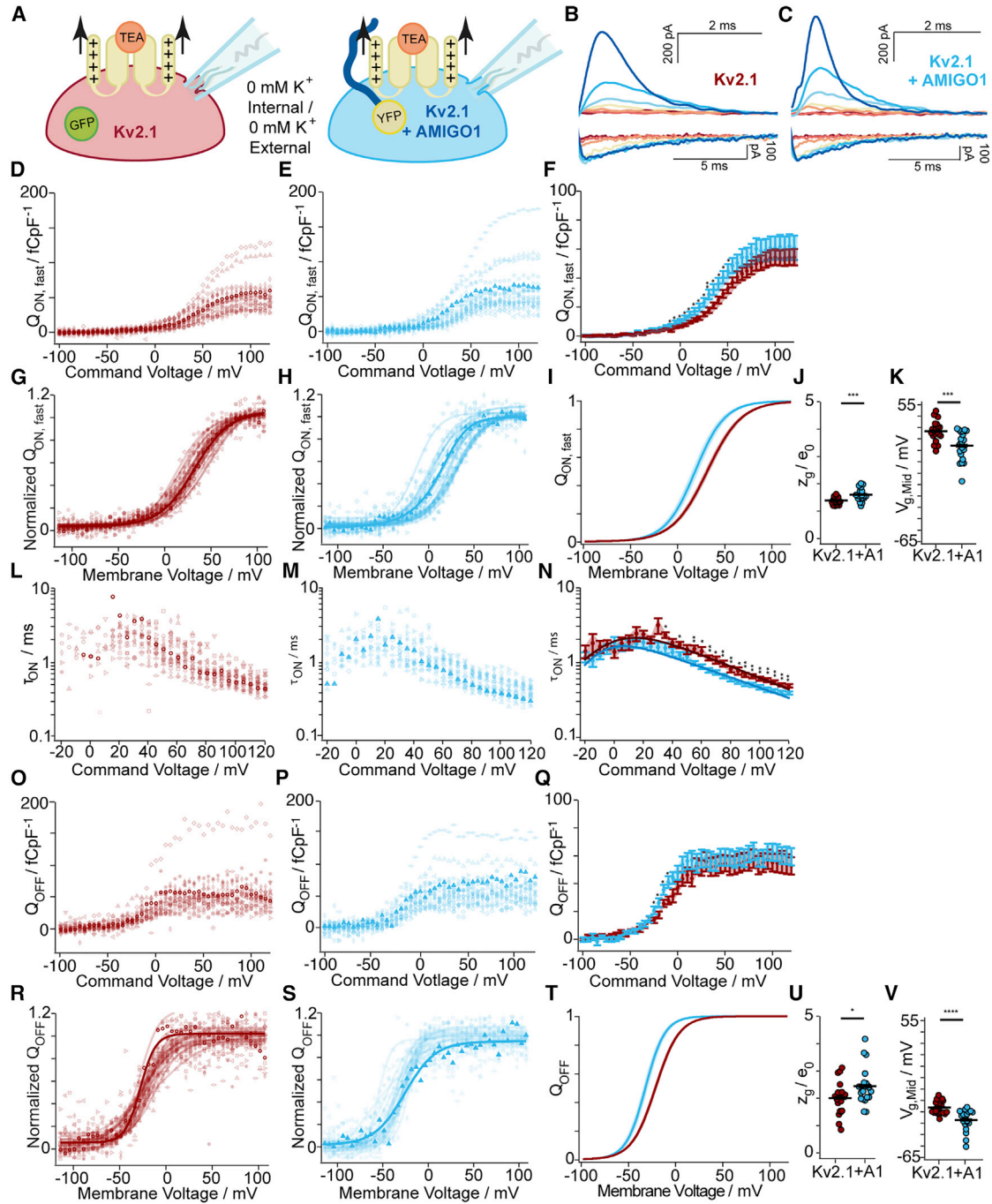


FIGURE 6 AMIGO1 facilitates the activation of Kv2 voltage sensors. (A) Experimental set up: gating currents (arrows) from Kv2.1-CHO transfected with GFP (red) or AMIGO1-YFP (blue). K^+ currents were eliminated by the removal of K^+ ions and the external tetraethylammonium, a Kv2 pore blocker (orange). (B and C) Top/bottom: representative $I_{g,ON}/I_{g,OFF}$ from Kv2.1-control (11.9 pF) or Kv2.1 + AMIGO1 (8.2 pF). Cells were given 100-ms voltage steps ranging from -100 (dark red trace) to +120 mV to record $I_{g,ON}$ and then stepped up to -140 mV to record $I_{g,OFF}$. The holding potential was -100 mV. Voltage pulses to -100, -50, -25, +0, +25, +50, and +100 mV are presented. Data points from representative cells are bolded in analysis panels. (D and E) $Q_{ON,fast}/pF-V$ relation from individual cells. $Q_{ON,fast}/pF$ is the gating charge integrated over the first 3.5 ms normalized to cell capacitance. (F) Mean $Q_{ON,fast}/pF$. (G and H) $Q_{ON,fast}-V$ relations normalized to maximum $Q_{ON,fast}$ from +50 to +100 mV voltage steps. Solid lines represent Boltzmann fit (Eq. 3). (I) Reconstructed Boltzmann fits from average $V_{g,Mid,ON,fast}$ and $z_{g,ON,fast}$ (Table 2). Shading $V_{g,Mid,ON,fast}$ mean \pm SEM. (J and K) Steepness (J) and midpoint (K) of Boltzmann fits. (L and M) τ_{ON} from individual cells fit with Eq. 8. (N) Average $\tau_{ON}-V$. Solid lines are Eq. 9 fit. Fit values \pm SD for Kv2.1-control cells: $\alpha_{0mV} = 254 \pm 26 \text{ s}^{-1}$, $z_g = 0.468 \pm 0.026 e_0$, $\beta_{0mV} = 261 \pm 50 \text{ ms}^{-1}$, $z_\beta = -1.31 \pm 0.37 e_0$; for Kv2.1 + AMIGO1 cells: $\alpha_{0mV} = 443 \pm 26 \text{ ms}^{-1}$, $z_g = 0.405 \pm 0.019 e_0$, $\beta_{0mV} = 157 \pm 52 \text{ ms}^{-1}$, $z_\beta = -2.00 \pm 0.55 e_0$. (O and P) Q_{OFF}/pF relation from individual cells normalized to cell capacitance. (Q) $Q_{OFF}/pF-V$ relation. (R and S) $Q_{OFF}-V$ relations normalized to maximum Q_{OFF} from +50 to +100 mV voltage steps. Solid lines are Boltzmann fits (Eq. 3). (T) Reconstructed Boltzmann fits using the average $V_{g,Mid,OFF}$ and $z_{g,OFF}$ (Table 2). Shading $V_{g,Mid,OFF}$ \pm SEM (U and V) Steepness (U) and midpoint (V) of Boltzmann fits. Mean \pm SEM. Statistics in Table 2. ****p = ≤ 0.0001 , ***p = ≤ 0.001 , **p = ≤ 0.01 , *p = ≤ 0.05 , ns, not significant. Bars are mean \pm SEM. To see this figure in color, go online.

of the total gating charge; the later charge movements, which include any charge associated with the pore opening, move too slowly for us to resolve accurately in ON measurements (4,5). If AMIGO1 acts solely through the pore, we would not expect to detect an impact on early components of ON-gating currents, which occur before pore opening.

At voltages above 50 mV, the charge density translocated over the first 3.5 ms, $Q_{ON,fast}$, was not significantly different with AMIGO1 (Fig. 6 D, E, and F), indicating that AMIGO1 did not alter the total charge translocated during early conformational transitions. However, between -10 and +50 mV, Kv2.1-control cells did not move as much gating charge as Kv2.1 + AMIGO1 cells, indicating a shift in gating-current activation (Fig. 6 F). The shift in voltage dependence was quantified by fitting $Q_{ON,fast}-V$ with a Boltzmann (Fig. 6 G, H, and I) yielding $\Delta V_{g,Mid,ON,fast}$ of -12.8 ± 3.5 mV (SEM) (Fig. 6 K) and a $\Delta z_{g,ON,fast}$ of $0.215 \pm 0.058 e_0$ (SEM) (Fig. 6 J) (Table 2). This result indicates that AMIGO1 modulates the early gating-charge movement, which occurs before pore opening.

To determine whether AMIGO1 modulates the kinetics of early gating-charge movement, we extracted a time constant (τ_{ON}) from the decay phase of $I_{g,ON}$ that occurs before 10 ms (Fig. 6 B, top, and C, top) (Eq. 8), as in (5). In Kv2.1 + AMIGO1 cells, the $\tau_{ON}-V$ relation shifts to more negative voltages compared with control (Fig. 6 L, M, and N). Above +30 mV, the mean τ_{ON} for Kv2.1 + AMIGO1 cells was faster than the mean τ_{ON} from Kv2.1-control cells (Fig. 6 N). Fitting the $\tau_{ON}-V$ with rate-theory equations indicated that AMIGO1 accelerates the forward rate of gating-charge movement by 1.7x at neutral voltage and decreases the voltage dependence of this rate by 13% (Fig. 6 N). This result indicates that voltage sensors activate faster in the presence of AMIGO1, consistent with destabilization of the earliest resting conformation of the voltage sensors by AMIGO1.

To measure if AMIGO1 alters the total gating-charge movement, we integrated OFF-gating currents ($I_{g,OFF}$) at -140 mV after 100-ms voltage steps (Fig. 6 B, bottom, C, bottom, O, P, and Q). The density of Q_{OFF} elicited by voltage steps above -10 mV was not significantly different between Kv2.1-control and Kv2.1 + AMIGO1 cells

(Fig. 6 Q), indicating that AMIGO1 did not alter the density of channels expressed nor the total gating charge per channel. However, between -25 and -10 mV, Kv2.1-control cells did not move as much gating charge as Kv2.1 + AMIGO1 cells, indicating a shift in voltage dependence (Fig. 6 Q). Boltzmann fits (Fig. 6 R, S, and T), yielded $\Delta V_{g,Mid,OFF}$ of -10.8 ± 2.4 mV (SEM) (Fig. 6 V) and a $\Delta z_{g,OFF}$ of $0.43 \pm 0.20 e_0$ (SEM) (Fig. 6 U) (Table 2), indicating that AMIGO1 shifts total gating-charge movement to more negative voltages. Overall, we find that AMIGO1 affects every aspect of gating current that we have analyzed to a greater degree than the K^+ conductance. As both $Q_{ON,fast}-V$ and α_{0mV} measurements report the gating-charge movements out of the earliest resting conformation, these results indicate that AMIGO1 destabilizes the earliest resting conformation relative to voltage-sensor conformations later in the conduction activation pathway of Kv2.1.

AMIGO1 accelerates voltage-stimulated GxTX-594 dissociation

To further test the hypothesis that AMIGO1 specifically destabilizes the earliest resting conformation of Kv2.1 voltage sensors, we probed the stability of this conformation with GxTX-594 fluorescence. The earliest resting conformation is stabilized by GxTX (5), and when occupancy of this conformation is decreased by voltage activation, the rate of GxTX-594 dissociation accelerates (45). Destabilization of the earliest resting conformation by AMIGO1 is expected to increase the rate of GxTX-594 dissociation when voltage sensors are partially activated. To test this prediction, we measured the rate of GxTX-594 dissociation at +30 mV, a potential at which about 20% of Kv2.1 gating charge is activated with GxTX bound (5). The rate of GxTX-594 dissociation from Kv2.1 ($k_{\Delta F}$) accelerated from $0.073 \pm 0.010 s^{-1}$ (SEM) in control cells to $0.115 \pm 0.015 s^{-1}$ (SEM) in cells positive for AMIGO1-YFP fluorescence (Fig. 7). As we see no evidence that AMIGO1 alters GxTX-594 affinity in cells at rest (Fig. S2), this 1.6-fold acceleration of $k_{\Delta F}$ is consistent with AMIGO1 destabilizing the earliest resting

TABLE 2 Boltzmann parameters and ΔG calculations for voltage-sensor movement

Kv2.1-CHO cells	$Q-V$ fit parameters				ΔG_{AMIGO1} (kcal/mol)		
	$Q_{ON,fast}$	$V_{g,Mid}$ (mV)	z_g (e_0)	n			
rKv2.1 + GFP		30.6 ± 2.0^S	1.38 ± 0.03^U	20			-1.92
rKv2.1 + AMIGO1-YFP		17.8 ± 2.9^T	1.61 ± 0.05^V	20			
Q_{OFF}	$V_{g,Med}$ (mV)	$V_{g,Med}$ (mV)	z_g (e_0)	n	Eq. 5	Eq. 11 ^a	Eq. 11 ^{a,b}
rKv2.1 + GFP	-22.0 ± 1.3^W	-19.5	2.00 ± 0.13^Y	20	-2.45	-3.11 ± 0.69	-2.74
rKv2.1 + AMIGO1-YFP	-32.8 ± 2.0^X	-29.0	2.43 ± 0.15^Z	20			

Average $V_{g,Mid}$ and z_g values were derived from first-order Boltzmann fits of n individual cells. Means \pm SEM. $V_{g,Med} = V_{g,1/2}$. $V_{g,Med}$ is median voltage (58). Unpaired, two-tailed t-test p values: $Q_{ON,fast}$: ST: 0.00093, UV: 0.00084. OFF-gating currents: WX: 7.82×10^{-5} , YZ: 0.038.

^a $z = 12.5 e_0$.

^b $V_{g,Med}$ was used.

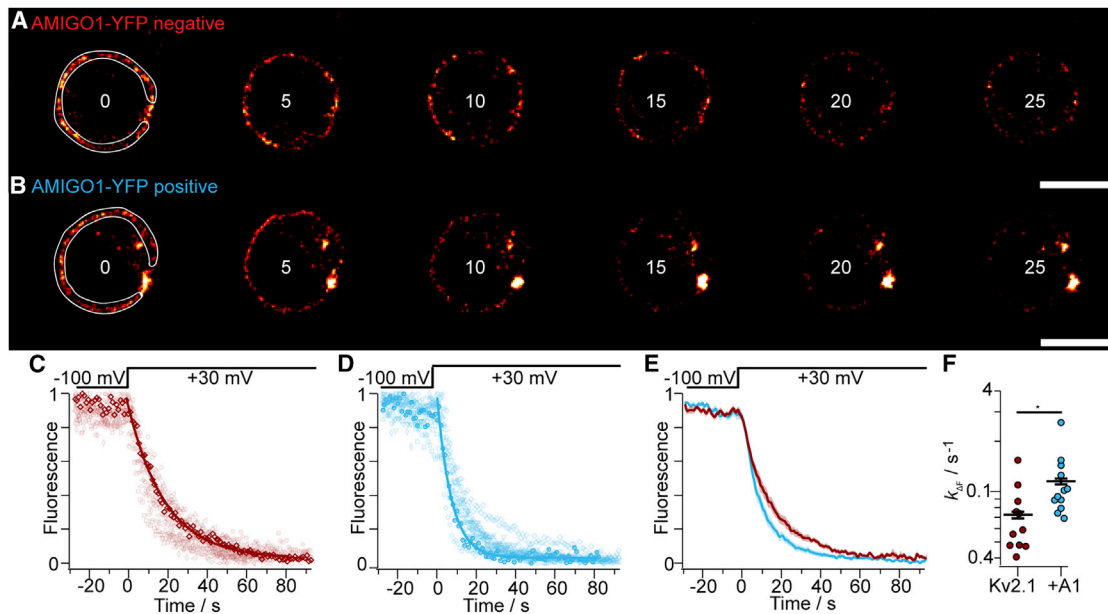


FIGURE 7 AMIGO1 accelerates voltage-stimulated GxTX-594 dissociation. (A and B) Fluorescence from the solution-exposed membrane of voltage-clamped Kv2.1-CHO cells \pm AMIGO1-YFP. Kv2.1 expression was achieved through a 48-h induction period. Cells were held at -100 mV for 30 s before being stimulated to +30 mV (time = 0 s) to trigger GxTX-594 dissociation. The time point in seconds of each image is listed. The region of interest for analysis is shown by the white line in left panel, which excludes the point contact with the pipette and the intracellular regions that have voltage-insensitive fluorescence. Scale bar, 10 μ m. (C and D) Normalized fluorescence intensity decay plots for Kv2.1-CHO cells without (red) and with (blue) AMIGO1-YFP fluorescence. The bolded traces correspond to exemplar cells in (A) and (B). Solid line is monoexponential fit (Eq. 7). (E) Averaged fluorescence intensity decay for AMIGO1-YFP negative (red) and AMIGO1-YFP positive (blue) cells. Mean \pm SEM is shaded. (F) Rates of fluorescence change ($k_{\Delta F}$) were calculated as $1/\tau$ from Eq. 7 fits. * $p = 0.03$ unpaired, two-tailed, t-test. To see this figure in color, go online.

conformation of voltage sensors. The thermodynamic model developed to interpret the $k_{\Delta F}$ of GxTX-594 dissociation (45) estimates that AMIGO1 decreases the stability of the earliest resting conformation of each voltage sensor by 1.9-fold or a ΔG_{AMIGO1} of -1.5 kcal/mol for Kv2.1 tetramers (Eq. 11). This result is consistent with AMIGO1 destabilizing the resting voltage-sensor conformation to speed up voltage-sensor activation and to shift conductance to lower voltages.

An extracellular surface-potential mechanism of AMIGO1 was not detected

To differentiate between mechanisms through which AMIGO1 could change voltage-sensor activation, we probed whether the large AMIGO1 extracellular domain is directly changing the electrostatic environment of Kv2.1's voltage sensors. Per surface-charge theory, local extracellular negative charges could attract positive gating charges to activate channels (73). AMIGO1 possesses five extracellular glycosylation sites (74), each potentially decorated with negatively charged sugar moieties (28). AMIGO1 also has a conserved negatively charged residue predicted to be near the extracellular side of the membrane (24,74). Similar structural characteristics are found in Nav β auxiliary subunits that, like AMIGO1, are glycosylated, single-transmembrane pass proteins with an immunoglob-

ulin domain. Nav β 1 has been proposed to interact with the Nav1.4 α -subunit through surface-charge effects (75–77). We tested if AMIGO1 likewise affects Kv2.1 activation through electrostatic surface-charge interactions.

To measure the electrostatics of the environment immediately surrounding the Kv2.1 VSD complex with and without AMIGO1, we employed far-red polarity-sensitive fluorescence (78). The polarity-sensitive fluorophore, JP, was localized to the Kv2.1 voltage sensor by conjugating GxTX to JP at either residue Ser13 or Lys27 (46). When GxTX binds to the extracellular S3b region of the Kv2.1 channel, Ser13 and Lys27 occupy positions of distinct polarity (46). At resting membrane potentials, GxTX Ser13Pra(JP) has an emission maximum of 644 nm, consistent with the homology-based prediction that Ser13 of GxTX localizes in an aqueous environment branched away from S4. Conversely, GxTX Lys27Pra(JP) has an emission maximum of 617 nm, consistent with the prediction that Lys27 sits in the polar region of the membrane adjacent to S4 (46). If AMIGO1 were to alter the electrostatic environment of the resting conformation of the Kv2.1 VSD, we would expect either of these environmental point detectors, GxTX Ser13Pra(JP) or GxTX Lys27Pra(JP), to exhibit an altered emission maximum.

Full emission spectra of JP fluorescence from Kv2.1-CHO cells transfected with AMIGO1-YFP and treated with GxTX Ser13Pra(JP) or GxTX Lys27Pra(JP) were fitted with 2-component split pseudo-Voigt functions

(Fig. 8 C and F). Fitting shows that the emission peaks, 644 and 617 nm, respectively, were unchanged with or without AMIGO1-YFP, consistent with the local electrostatic environment surrounding the JP probes positioned on resting Kv2.1 voltage sensors not being altered by AMIGO1 expression. Previous work has shown that the GxTX Lys27Pra(JP) emission-peak wavelength is sensitive to conformational changes among early resting states of voltage sensors (46). The absence of any AMIGO1-induced change in the environment for either of these GxTX side chains suggests that AMIGO1 does not cause significant changes to the local environment of the GxTX binding site on the S3b segment of Kv2.1 nor the GxTX position in the membrane when bound to the channel. These results are consistent with destabilization of the GxTX binding site by AMIGO1 being indirect, as the binding site itself appears to retain the same conformation and local environment in the presence of AMIGO1. However, it remains possible that AMIGO1 acts extracellularly to modulate Kv2.1 by a mechanism that these GxTX(JP)-based sensors do not detect.

We also tested whether AMIGO1 acts by a surface-charge mechanism with a classical charge-screening approach. Surface-charge interactions can be revealed by increasing the concentration of Mg^{2+} to minimize, or screen, the impact of fixed negative charges near the voltage sensors (73,79). If AMIGO1 alters surface potential, we would expect elevated Mg^{2+} to shrink $\Delta V_{i, Mid}$. To determine whether surface-charge screening suppresses the AMIGO1 effect,

voltage-clamp experiments were conducted as in Fig. 3, except external recording solutions contained 100 mM Mg^{2+} (Fig. 9 A, B, and C). Kv2.1 requires more positive voltage steps to activate in high Mg^{2+} solutions (Table 1), consistent with sensitivity to surface-charge screening (80). In high Mg^{2+} , AMIGO1 effected a $\Delta V_{i, Mid}$ of -7.4 ± 2.4 mV (SEM) (Fig. 10 H) but did not change z_i (Fig. 9 G) (Table 1). When compared with low Mg^{2+} conditions by ordinary 2-way analysis of variance, $\Delta V_{i, Mid}$ was not significantly different in normal versus 100 mM Mg^{2+} (interaction of $p = 0.33$). Hence, Mg^{2+} altered Kv2.1 activation in a manner consistent with surface-charge screening, yet Mg^{2+} did not detectably abrogate the AMIGO1 effect. However, a surface-charge site could be insensitive to 100 mM Mg^{2+} . It remains a possibility that other manipulations, such as altering AMIGO1 glycosylation, could reveal that AMIGO1 surface charge impacts Kv2.1 gating. While neither extracellular fluorescence measurements nor surface-charge screening detected an extracellular impact of AMIGO1, we are not able to rule out the possibility of an extracellular coupling to AMIGO1 that was not detected by these methods.

DISCUSSION

We asked whether AMIGO1 modulates Kv2.1 conductance by modulating conformational changes of pore opening or voltage-sensor activation. We found that AMIGO1 destabilizes the resting, inward conformation of Kv2.1 voltage

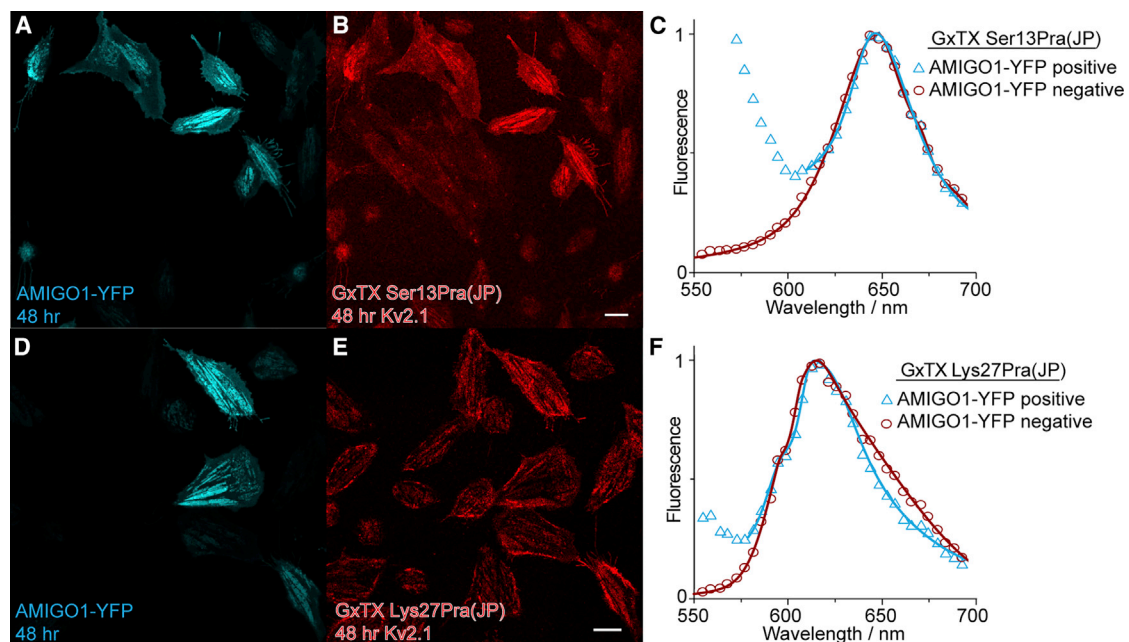


FIGURE 8 AMIGO1 does not alter the Kv2.1–GxTX interface on resting voltage sensors. Kv2.1–CHO cells transfected with AMIGO1-YFP were treated with GxTX Ser13Pra(JP) or GxTX Lys27Pra(JP). (A, B, D, and E) Confocal image of AMIGO1-YFP fluorescence (blue) (A and D) and JP fluorescence (B and E). (C and F) Fitted emission spectra of cells positive (blue) and negative (red) for AMIGO1-YFP fluorescence. Data points for all spectra are the mean of normalized emission from AMIGO1-YFP-positive cells and AMIGO1-negative cells. Spectra were fit with two-component split pseudo-Voigt functions with shape parameters and root-mean-squared values found in Table S1. To see this figure in color, go online.

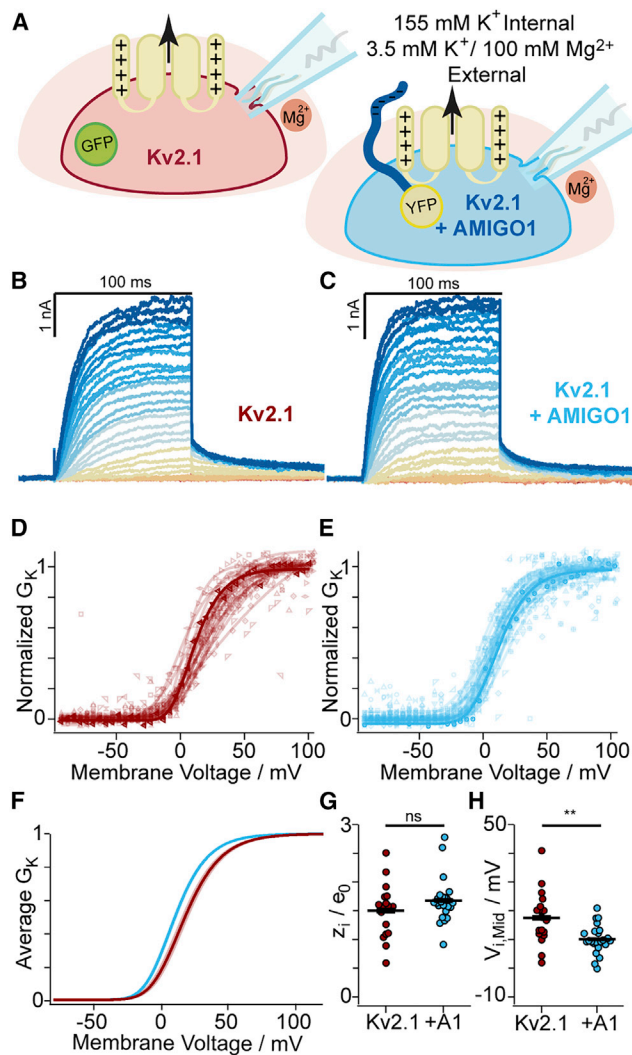


FIGURE 9 Surface-charge screening does not suppress the AMIGO1 effect. (A) Experimental set up: whole-cell K^+ currents (arrow) from Kv2.1–CHO transfected with GFP (red) or AMIGO1-YFP (blue). 100 mM magnesium was used to shield surface charges (peach halo). Same voltage protocol and representations as Fig. 3. (B and C) Representative Kv2.1-control (10.0 pF) or Kv2.1 + AMIGO1 (6.3 pF) cells. (D and E) Normalized G – V relationships. (F) Reconstructed fourth-order Boltzmann fits from average $V_{i, \text{Mid}}$ and z_i (Table 1). Shading $V_{i, \text{Mid}} \pm \text{SEM}$. (G and H) Steepness (G) and midpoint (H) of fourth-order Boltzmann fits. Mean \pm SEM. Statistics in Table 1. ** $p \leq 0.01$, ns, not significant. To see this figure in color, go online.

sensors, causing channels to activate at more negative voltages. This conclusion is supported by three major results.

AMIGO1 destabilizes the earliest resting conformation of Kv2.1 voltage sensors

AMIGO1 expression accelerated conductance activation only at a subset of voltages where the activation kinetics are voltage sensitive (Fig. 3 M). When voltage-sensor movements were measured directly, gating-current recordings revealed an acceleration of the forward rate constant

(τ_{ON}) of gating-charge activation in cells with AMIGO1. Between 0 and 120 mV, pore opening is 10–30 times slower than $I_{g, \text{ON}}$ decay (Figs. 3 M and 6 N), too slow to influence the first few ms of $I_{g, \text{ON}}$. When the change in the forward rate α_{0mV} (Fig. 6 N) was used to estimate the amount of energy AMIGO1 contributes to modulating Kv2.1 conformational bias, we found that AMIGO1 imparted -1.3 kcal/mol per channel (Eq. 10) to $\Delta G_{\text{AMIGO1}}^\ddagger$. From this result, we conclude that AMIGO1 speeds the rate of conformational change between the earliest resting conformation and its transition state in the activation path. Additionally, the AMIGO1 effect on GxTX-594 dissociation at +30 mV is consistent with AMIGO1 opposing the action of GxTX-594, which stabilizes resting voltage sensors. All available evidence indicates that AMIGO1 destabilizes the earliest resting conformation of Kv2.1 voltage sensors. We estimate that AMIGO1 destabilizes the fully resting conformation of Kv2.1 channels by ~ 3 kcal/mol, relative to the fully active open state, and that about half of this energy lowers the barrier for the initial exit of voltage sensors from their resting conformation (Fig. 10 A).

AMIGO1 has a greater impact on the voltage sensors than the pore opening

Free energy estimates indicate more AMIGO1 perturbation of the Q – V than the midpoint of the G – V . The ΔG for AMIGO1's impact on voltage-sensor activation ranged from -1.9 to -3.1 kcal/mol depending on the calculation method (Table 2). Yet, the ΔG_{AMIGO1} calculated at the conductance midpoint was only -0.3 kcal/mol (Table 1). This lesser impact on pore opening is consistent with a direct impact of AMIGO1 on voltage-sensor movements, which are coupled to pore opening. Notably ΔG_{AMIGO1} calculated at the conductance midpoint widens to -0.8 kcal/mol when voltage-sensor activation is limited with GxTX-594. When we looked at pore opening directly, we saw no evidence suggesting a direct effect of AMIGO1. We saw no change in the slope of the G – V relationship with AMIGO1 (Table 1), nor sigmoidicity (Fig. 3), nor single-channel measurements (Fig. 4). While these negative results do not eliminate the possibility that AMIGO1 has a small direct effect on pore opening, they do constrain the effect size of AMIGO1 on pore-opening equilibria to be smaller than the error associated with our measurements.

The AMIGO1 impact on conductance is malleable

In Kv2.1–CHO cells, AMIGO1 shifts the V_{Mid} of conductance by -5.7 ± 2.2 mV (SEM). With GxTX-594, the AMIGO1 G – V shift widens to -22.3 ± 4.8 (SEM) (Table 1). This remarkable result indicates that the AMIGO1 effect on conductance can change in magnitude. While we have not completely excluded the possibility that AMIGO1 has a

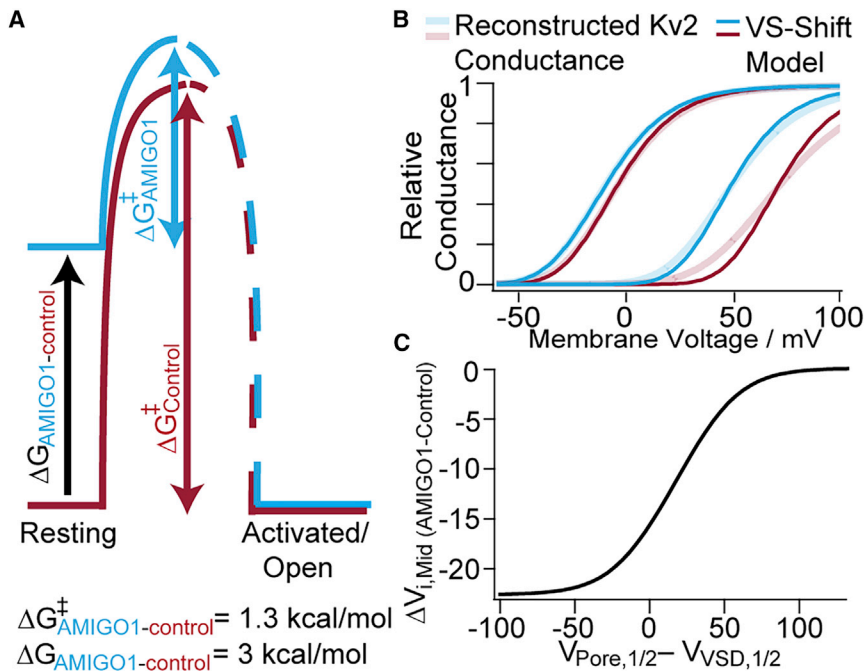


FIGURE 10 AMIGO1 destabilizes the resting conformation of Kv2.1 voltage sensors. (A) AMIGO1 raises resting-state energy (ΔG) of Kv2.1 voltage sensors and lowers the energy barrier (ΔG^{\ddagger}) of Kv2.1 activation. (B) Voltage-sensor-shift model of AMIGO1 modulation (dark lines) plotted with reconstructed G - V s from Kv2.1-CHO Table 1 values (pale lines). From left to right: Kv2.1 + AMIGO1, Kv2.1-control, Kv2.1 + AMIGO1 with GxTX-594, and Kv2.1-Control with GxTX-594. The voltage-sensor-shift model is $f(V) = \left(1 + e^{-(V-V_{\text{VSD},1/2})} (z/25.46)\right)^{-4} \cdot \left(1 + e^{-(V-V_{\text{Pore},1/2})} (z/25.46)\right)^{-1}$, where $z = 1.5 e_0$, $V_{\text{Pore},1/2} = -16 \text{ mV}$, and $V_{\text{VSD},1/2}$ varies. Kv2.1-control $V_{\text{VSD},1/2} = -33 \text{ mV}$ and Kv2.1-control with GxTX-594 $V_{\text{VSD},1/2} = 51 \text{ mV}$. AMIGO1 $\Delta V_{\text{VSD},1/2} = -22 \text{ mV}$ with or without GxTX-594. (C) Dependence of AMIGO1 G - V midpoint shift ($\Delta V_{i,\text{Mid}}$) on $V_{1/2}$ of pore in relation to $V_{1/2}$ VSD in model from (B). In this panel, $\Delta V_{i,\text{Mid}}$ is where $f(V) = 0.5$. To see this figure in color, go online.

direct interaction with GxTX-594, we think this unlikely, as we saw no sign of an AMIGO1-dependent environmental change around GxTX-JP conjugates, and GxTX-594 had a similar affinity for resting Kv2.1. We think it is more likely that AMIGO1 and GxTX-594 interact only allosterically, and we favor the explanation that GxTX makes the $V_{i,\text{Mid}}$ of conductance more sensitive to the early voltage-sensor transition, which AMIGO1 modulates. After its fast voltage-sensor movement, Kv2.1 has a slow conductance-activating step that makes the fourth power of the Q - V not predictive of the G - V (3–5,57). GxTX stabilizes the earliest resting conformation of Kv2.1 voltage sensors such that fourth-power Boltzmann fits to the G - V are similar to the Q - V (5). This suggests the $V_{i,\text{Mid}}$ is more responsive to AMIGO1 in GxTX-594 because the G - V becomes limited by early voltage-sensor movement.

To test the idea that AMIGO1 modulation of voltage sensors could result in different $\Delta V_{i,\text{Mid}}$ of G - V s, we performed calculations with a voltage-sensor-shift model composed of simple gating equations. This voltage-sensor-shift model incorporates distinct $V_{1/2}$ values assigned to independent voltage-sensor ($V_{\text{VSD},1/2}$) and pore ($V_{\text{Pore},1/2}$) transitions, all of which must activate to allow channel opening. Calculations incorporating a constant $\Delta V_{\text{VSD},1/2}$ shift with no change in $V_{\text{Pore},1/2}$ demonstrate that the $\Delta V_{i,\text{Mid}}$ of G - V can be malleable. In these calculations, an AMIGO1 shift of $\Delta V_{\text{VSD},1/2} = -22.4 \text{ mV}$ resulted in $\Delta V_{i,\text{Mid}} = -5.0 \text{ mV}$ (Fig. 10 B), similar to the empirical measurement $\Delta V_{i,\text{Mid}} = -5.7 \text{ mV}$ of Kv2.1 with AMIGO1 (Fig. 3). However, when $V_{\text{VSD},1/2}$ was modified to fit GxTX-594 data, this same AMIGO1 shift of $\Delta V_{\text{VSD},1/2} = -22.4 \text{ mV}$ yielded a larger shift

G - V shift, $\Delta V_{i,\text{Mid}} = -21.8 \text{ mV}$ (Fig. 10 B). While the gating model implied by these calculations is highly simplified and does not recapitulate all of our data, it does demonstrate a mechanism by which a fixed modulation of voltage sensors could result in varying $\Delta V_{i,\text{Mid}}$ shifts. As the voltage dependence of Kv2.1 activation is dynamically modulated by many forms of cellular regulation and can vary dramatically (16–20,81–86), the impact of AMIGO1 might also fluctuate. We conducted an analysis of gating-parameter combinations in our highly simplified model and found a maximal AMIGO1 G - V shift when the pore transition occurs at more negative potentials than voltage-sensor activation (Fig. 10 C). While the magnitude and precise voltage response of the AMIGO1 gating shift depend on specific gating parameters and the structure of the model, a general principle underlies this gating-parameter dependence: if, at the G - V midpoint, channel opening is limited by voltage sensors occupying an AMIGO1-sensitive resting conformation, then the G - V midpoint will be very sensitive to AMIGO1; however, if almost all voltage sensors have already exited resting conformations at the G - V midpoint, then AMIGO1 destabilization of resting conformations will have little impact. A malleable impact of AMIGO1 in response to regulation of voltage-sensor or pore transitions could perhaps explain why a larger Kv2.1 G - V shift was originally reported (22) than was observed here or elsewhere (23).

The voltage-sensor-shift mechanism we propose does not require changes in pore opening or voltage sensor-pore coupling. Maverick and colleagues (23) suggested that the effects of AMIGO proteins on Kv2.1 conductance could be described by increasing the coupling between the voltage

sensor and pore opening without a shift in the $Q-V$ curve (23), similar to a mechanism by which leucine-rich-repeat-containing protein 26, LRRC26, modulates large-conductance Ca^{2+} -activated K^+ channels (37). As the precise voltage sensor-pore coupling mechanisms for Kv2.1 channels have yet to be defined, we cannot rule out the possibility that AMIGO1 also alters coupling. However, we see no reason that AMIGO1 must do anything other than destabilize the earliest resting conformation of voltage sensors to modulate Kv2.1 conductance.

Limitations

More detailed investigation of the AMIGO1 impact on the Kv2.1 activation pathway was limited by the relatively small magnitude of AMIGO1-dependent effects versus the cell-to-cell variability, with $\Delta V_{i,\text{Mid}}$ as low as 5 mV, and standard deviations for $V_{i,\text{Mid}}$ of 4–9 mV (Table 1; excluding GxTX-594). While we compensated for the limited power of the AMIGO1 effect by increasing replicates, a decreased cell-to-cell variability would enable more precise biophysical investigation. This degree of cell-to-cell variability does not appear to be unique to our laboratory. Midpoints reported for rat Kv2.1 activation in HEK293 cells span a 36-mV range, from -20.2 to 16.4 mV (22,23,67,72,87–95). When we calculated V_{Mid} standard-deviation values from the standard errors and n values in these studies, standard deviations ranged from 1 to 17 mV, on par with our own. We suspect these notable V_{Mid} deviations result from the many different types of regulation to which Kv2.1 channels are susceptible (20,21). Techniques to constrain the cell-to-cell variability in Kv2.1 function could allow more precise mechanistic studies of AMIGO1 modulation.

Our interpretations assume that the AMIGO1 effect is similar whether Kv2.1 is expressed at low density to measure K^+ currents or at high density for gating-current and imaging experiments. Auxiliary subunit interactions with pore α subunits can be influenced by many factors that can alter their assembly and functional impact on channel currents (96–101). However, if Kv2.1 channels in K^+ -current recordings were modulated less by AMIGO1, we would expect a decrease in Boltzmann slope of the fit, a bimodal $G-V$ relation, or increased cell-to-cell variability with AMIGO1. We do not observe any of these with CHO cells. The similar impact of AMIGO1 on Kv2.1 conductance in two cell lines (Table 1) and consistency in effect magnitudes with an independent report (23) further suggest that the AMIGO1 effect is saturating in our K^+ -conductance measurements. Thus, while incomplete complex assembly and other factors could in theory influence the magnitude of the AMIGO1 impact on Kv2.1 conductance, we do not see evidence that would negate our biophysical assessment of the mechanism through which AMIGO1 alters Kv2.1 conductance.

The most parsimonious explanation for the effect AMIGO1 has on the Kv2.1 conduction-voltage relation

seems to be a direct interaction with Kv2.1 voltage sensors. However, it also seems possible that AMIGO1 proteins could change cellular regulation of which in turn modulates Kv2.1. Even if AMIGO1 acts by an indirect mechanism, our mechanistic conclusions remain valid, as they are not predicated on a direct protein-protein interaction between AMIGO1 and Kv2.1.

Potential physiological consequences of an AMIGO1 gating shift

AMIGO1 knockout mice display schizophrenia-related features (25), and AMIGO1 knockdown zebrafish have deformed neural tracts (26). The underpinnings of these deficits are unclear, as AMIGO1 modulates extracellular adhesion and Kv2 proteins and could have additional functions. AMIGO1 knockout results in $\sim 50\%$ decrease of Kv2.1 protein in mouse brain lysate (25). It is possible that the main effect of AMIGO-1 on Kv2.1 channels in the brain is related to trafficking, subcellular localization, or complex formation with other relevant modulatory proteins, which could alter Kv2-conductance density or nonconducting functions of Kv2 proteins (28,67,102–105). In our data set, transient transfection of AMIGO1 increased Kv2.1 current density in HEK cells, but not CHO cells (Fig. S5), and Kv2.1 gating-charge density remained similar in CHO cells \pm AMIGO1 (Fig. 6), suggesting that the AMIGO1 mechanism altering neuronal Kv2.1 protein expression *in vivo* was not recapitulated in CHO cells. Changes in Kv2 current density can modulate neuronal firing (7,10,106–108) and could conceivably contribute to AMIGO1 neurological phenotypes. The AMIGO1 shift of Kv2-conductance activation to more negative voltages could act in tandem with an increase in channel density. AMIGO1 co-localizes with seemingly all the Kv2 proteins in mammalian brain neurons (22,28,109), and in hippocampal pyramidal neurons from AMIGO1 knockout mice, a component of K^+ conductance activates at more negative voltages than wild type (25). While we can only speculate about which AMIGO1 actions produce phenotypes, we can consider the expected impact of AMIGO1-mediated gating changes on activation of neuronal Kv2 conductance.

In mammalian neurons, Kv2 conductance can speed action-potential repolarization (7,110), dampen the fast afterdepolarization phase (110), deepen trough voltage, and extend afterhyperpolarization (7) to impact repetitive firing (7,110–113). To estimate the impact AMIGO1 might have on the Kv2 conductance activated by an action potential, we superimposed the impact of AMIGO1 measured in Kv2.1-CHO cells onto the Kv2 conductance in rat superior cervical ganglion (SCG) neurons, which Liu and Bean (7) found to account for $\sim 55\%$ of outward current during an action potential. We roughly approximated an SCG action potential as a 1.5-ms step to 0 mV, during which the parameters fit by Liu and Bean predict

2.2% of the maximal Kv2 conductance will be activated. If the Kv2 parameters are modified to mimic removal of AMIGO1, SCG neuron Kv2 conductance at the end of the mock action potential decreases by 70% (Table 3). This large effect due to small changes in conductance activation suggests that the AMIGO1 gating shift could have a profound impact on electrical signaling. Furthermore, we think the AMIGO1 impact could be even greater. Liu and Bean found that in SCG neurons, Kv2 activation lacks the slow pore-opening step we see in Kv2.1-CHO cells, and SCG Kv2 kinetics were effectively modeled by a Hodgkin-Huxley n^4 model of activation (114). This suggests that only voltage-sensor activation limits conductance activation in the SCG neurons, maximizing the impact of the voltage sensors on AMIGO1 $\Delta V_{i, \text{Mid}}$. When the AMIGO1 $\Delta V_{i, \text{Mid}}$ of Kv2.1-CHO voltage sensors are applied to SCG neuron parameters, Kv2 conductance at the end of the mock action potential decreases by 89% (Table 3). Although speculative, this analysis suggests that eliminating the AMIGO1 impact on channel activation could be functionally equivalent to eliminating the majority of neuronal Kv2 current activated during an action potential.

CONCLUSIONS

To shift the activation midpoint of Kv2.1 conductance to lower voltages, AMIGO1 destabilizes the earliest resting conformations of Kv2.1 voltage sensors relative to more activated conformations. While we cannot rule out a direct influence on pore dynamics, we saw no indication of such. We propose that AMIGO1 shifts the voltage dependence of Kv2.1 conduction to more negative voltages by modulating early voltage-sensor movements.

We also propose that because AMIGO1 acts on early voltage-sensor movements, modulation of Kv2 gating can alter the impact of AMIGO1 on K^+ conductance.

TABLE 3 Prediction of AMIGO1 impacts on Kv2 conductance in superior cervical ganglion neurons

Calculated activation of native Kv2 conductance after 1.5 ms at 0 mV			
Type of AMIGO1 impact	τ_{0mV} (s)	V_{Mid} (mV)	Relative conductance
None, values from (7)	0.0029	-13.1	0.022
From conductance data	0.0040	-7.1	0.0067
From voltage-sensor data	0.0050	-2.3	0.0024

Liu and Bean fit Kv2 kinetics with $(1 - e^{-t/\tau_{0mV}})^4$ and the $G-V$ with $(1 + e^{-(V-V_{\text{Mid}})/k})^{-1}$, and these equations are used to calculate relative conductance. Here, τ_{0mV} and ΔV_{Mid} are adjusted for the impact of loss of AMIGO1 from Kv2.1-CHO cells. The AMIGO1 impact on conductance activation was a 1.38-fold acceleration of τ_{0mV} (Fig. 3 M) and $G-V$ $\Delta V_{i, \text{Mid}} = -5.7$ mV (Table 1). The AMIGO1 impact on voltage-sensor activation was a 1.74-fold acceleration of τ_{0mV} (change in α_{0mV} from fit in Fig. 6 N) and $Q_{\text{OFF}}-V$ $\Delta V_{g, \text{Mid}} = -10.8$ mV (Table 2).

SUPPORTING MATERIAL

Supporting material can be found online at <https://doi.org/10.1016/j.bpj.2022.03.020>.

AUTHOR CONTRIBUTIONS

R.J.S., conceptualization, data curation, formal analysis, funding acquisition, investigation, methodology, project administration, visualization, writing – original draft, and writing – review & editing; R.G.S., formal analysis and visualization; L.A.V., formal analysis and visualization; P.T., resources; Z.W., resources; B.E.C., conceptualization, funding acquisition, project administration, and writing – review & editing; J.T.S., conceptualization, funding acquisition, investigation, methodology, project administration, supervision, writing – original draft, and writing – review & editing.

ACKNOWLEDGMENTS

We thank Vladimir Yarov-Yarovoy, James Trimmer, Karen Zito, and Tsung-Yu Chen of the University of California Davis (UC Davis) for constructive feedback integral to the design and synthesis of experimental ideas. The authors would like to thank the UC Davis statisticians Drs. Sandra Taylor and Susan Stewart as well as Karl Brown for their consultation on statistical approaches. This research was funded by National Institutes of Health grants T32GM007377 (R.J.S.), F31NS108614 (R.J.S.), R01NS096317 (J.T.S. and B.E.C.), and R21EY026449 (J.T.S.). The GxTX-Ser13Cys, GxTX-Ser13-Pra, and GxTX-Lys27Pra peptides were synthesized at the Molecular Foundry of the Lawrence Berkeley National Laboratory under US Department of Energy contract DE-AC02-05CH11231. The authors declare no competing financial interests.

REFERENCES

- Kihira, Y., T. O. Hermanstynne, and H. Misonou. 2010. Formation of heteromeric Kv2 channels in mammalian brain neurons. *J. Biol. Chem.* 285:15048–15055.
- Long, S. B., X. Tao, ..., R. MacKinnon. 2007. Atomic structure of a voltage-dependent K⁺ channel in a lipid membrane-like environment. *Nature.* 450:376–382.
- Islas, L. D., and F. J. Sigworth. 1999. Voltage sensitivity and gating charge in Shaker and Shab family potassium channels. *J. Gen. Physiol.* 114:723–742.
- Scholle, A., S. Dugarmaa, ..., K. Benndorf. 2004. Rate-limiting reactions determining different activation kinetics of Kv1.2 and Kv2.1 channels. *J. Membr. Biol.* 198:103–112.
- Tilley, D. C., J. M. Angueyra, ..., J. T. Sack. 2019. The tarantula toxin GxTx detains K⁺ channel gating charges in their resting conformation. *J. Gen. Physiol.* 151:292–315.
- Du, J., L. L. Haak, ..., C. J. McBain. 2000. Frequency-dependent regulation of rat hippocampal somato-dendritic excitability by the K⁺ channel subunit Kv2.1. *J. Physiol.* 522 (Pt 1):19–31.
- Liu, P. W., and B. P. Bean. 2014. Kv2 channel regulation of action potential repolarization and firing patterns in superior cervical ganglion neurons and hippocampal CA1 pyramidal neurons. *J. Neurosci.* 34:4991–5002.
- Malin, S. A., and J. M. Nerbonne. 2002. Delayed rectifier K currents, IK, are encoded by Kv2-subunits and regulate tonic firing in mammalian sympathetic neurons. *Mol. Biol.* 22:10094–10105.
- Hönigsperger, C., M. J. Nigro, and J. F. Storm. 2017. Physiological roles of Kv2 channels in entorhinal cortex layer II stellate cells revealed by Guanyxitoxin-1E. *J. Physiol.* 595:739–757.

10. Romer, S. H., A. S. Deardorff, and R. E. W. Frye. 2019. A molecular rheostat: Kv2.1 currents maintain or suppress repetitive firing in motoneurons. *J. Physiol.* 597:3769–3786.
11. Vacher, H., D. P. Mohapatra, and J. S. Trimmer. 2008. Localization and targeting of voltage-dependent ion channels in mammalian central neurons. *Physiol. Rev.* 88:1407–1447.
12. Specia, D. J., G. Ogata, ..., J. S. Trimmer. 2014. Deletion of the Kv2.1 delayed rectifier potassium channel leads to neuronal and behavioral hyperexcitability. *Genes, Brain Behav.* 13:394–408.
13. Kang, S. K., C. G. Vanoye, ..., J. A. Kearney. 2019. Spectrum of K(v) 2.1 dysfunction in KCNB1-associated neurodevelopmental disorders. *Ann. Neurol.* 86:899–912.
14. Torkamani, A., K. Bersell, ..., J. A. Kearney. 2014. De novo KCNB1 mutations in epileptic encephalopathy. *Ann. Neurol.* 76:529–540.
15. Thiffault, I., D. J. Specia, ..., J. T. Sack. 2015. A novel epileptic encephalopathy mutation in KCNB1 disrupts Kv2.1 ion selectivity, expression, and localization. *J. Gen. Physiol.* 146:399–410.
16. Misonou, H., M. Menegola, ..., J. S. Trimmer. 2006. Bidirectional activity-dependent regulation of neuronal ion channel phosphorylation. *J. Neurosci.* 26:13505–13514.
17. Misonou, H., D. P. Mohapatra, ..., J. S. Trimmer. 2005. Calcium- and metabolic state-dependent modulation of the voltage-dependent Kv2.1 channel regulates neuronal excitability in response to ischemia. *J. Neurosci.* 25:11184–11193.
18. Aras, M. A., R. A. Saadi, and E. Aizenman. 2009. Zn²⁺ regulates Kv2.1 voltage-dependent gating and localization following ischemia. *Eur. J. Neurosci.* 30:2250–2257.
19. Misonou, H., S. M. Thompson, and X. Cai. 2008. Dynamic regulation of the Kv2.1 voltage-gated potassium channel during brain ischemia through neuroglial interaction. *J. Neurosci.* 28:8529–8538.
20. Murakoshi, H., G. Shi, ..., J. S. Trimmer. 1997. Phosphorylation of the Kv2.1 K⁺ channel alters voltage-dependent activation. *Mol. Pharmacol.* 52:821–828.
21. Plant, L. D., E. J. Dowdell, ..., S. A. N. Goldstein. 2011. SUMO modification of cell surface Kv2.1 potassium channels regulates the activity of rat hippocampal neurons. *J. Gen. Physiol.* 137:441–454.
22. Peltola, M. A., J. Kuja-Panula, ..., H. Rauvala. 2011. AMIGO is an auxiliary subunit of the Kv2.1 potassium channel. *EMBO Rep.* 12:1293–1299.
23. Maverick, E. E., A. N. Leek, and M. M. Tamkun. 2021. Kv2 channel/AMIGO β -subunit assembly modulates both channel function and cell adhesion molecule surface trafficking. *J. Cell Sci.* 134:jcs256339.
24. Kuja-Panula, J., M. Kiiltomäki, ..., H. Rauvala. 2003. AMIGO, a transmembrane protein implicated in axon tract development, defines a novel protein family with leucine-rich repeats. *J. Cell Biol.* 160:963–973.
25. Peltola, M. A., J. Kuja-Panula, ..., H. Rauvala. 2015. AMIGO-Kv2.1 potassium channel complex is associated with schizophrenia-related phenotypes. *Schizophr. Bull.* 42:105.
26. Zhao, X., J. Kuja-Panula, ..., H. Rauvala. 2014. Amigo adhesion protein regulates development of neural circuits in zebrafish brain. *J. Biol. Chem.* 289:19958–19975.
27. Chen, Y., H. H. Hor, and B. L. Tang. 2012. AMIGO is expressed in multiple brain cell types and may regulate dendritic growth and neuronal survival. *J. Cell. Physiol.* 227:2217–2229.
28. Bishop, H. I., M. M. Cobb, ..., J. S. Trimmer. 2018. Kv2 ion channels determine the expression and localization of the associated AMIGO-1 cell adhesion molecule in adult brain neurons. *Front. Mol. Neurosci.* 11:1.
29. Cregg, R., B. Laguda, ..., M. Kinali. 2013. Novel mutations mapping to the fourth sodium channel domain of nav1.7 result in variable clinical manifestations of primary erythromelalgia. *NeuroMolecular Med.* 15:265–278.
30. Huang, J., M. Estacion, ..., S. D. Dib-Hajj. 2019. A novel gain-of-function Nav1.9 mutation in a child with episodic pain. *Front. Neurosci.* 13:1–11.
31. Abriel, H., C. Cabo, ..., R. S. Kass. 2001. Novel arrhythmogenic mechanism revealed by a long-QT syndrome mutation in the cardiac Na⁺ channel. *Circ. Res.* 88:740–745.
32. Dudem, S., R. J. Large, ..., M. A. Hollywood. 2020. LINGO1 is a regulatory subunit of large conductance, Ca²⁺-activated potassium channels. *Proc. Natl. Acad. Sci. U S A.* 117:2194–2200.
33. Rockman, M. E., A. G. Vouga, and B. S. Rothberg. 2020. Molecular mechanism of BK channel activation by the smooth muscle relaxant NS11021. *J. Gen. Physiol.* 152:e201912506.
34. Horrigan, F. T., and R. W. Aldrich. 2002. Coupling between voltage sensor activation, Ca²⁺ binding and channel opening in large conductance (BK) potassium channels. *J. Gen. Physiol.* 120:267–305.
35. Zhu, W., T. L. Voelker, ..., J. R. Silva. 2017. Mechanisms of noncovalent β subunit regulation of NaV channel gating. *J. Gen. Physiol.* 149:813–831.
36. Barro-Soria, R., M. E. Perez, and H. P. Larsson. 2015. KCNE3 acts by promoting voltage sensor activation in KCNQ1. *Proc. Natl. Acad. Sci. U S A.* 112:E7286–E7292.
37. Yan, J., and R. W. Aldrich. 2010. LRRC26 auxiliary protein allows BK channel activation at resting voltage without calcium. *Nature.* 466:513–516.
38. Barro-Soria, R., R. Ramentol, ..., H. P. Larsson. 2017. KCNE1 and KCNE3 modulate KCNQ1 channels by affecting different gating transitions. *Proc. Natl. Acad. Sci. U S A.* 114:E7367–E7376.
39. Nakajo, K., and Y. Kubo. 2015. KCNQ1 channel modulation by KCNE proteins via the voltage-sensing domain. *J. Physiol.* 593:2617–2625.
40. Zhang, J., and J. Yan. 2014. Regulation of BK channels by auxiliary γ subunits. *Front. Physiol.* 5:401.
41. Brackenbury, W. J., and L. L. Isom. 2011. Na⁺ channel β subunits: overachievers of the ion channel family. *Front. Pharmacol.* 2:1–11.
42. Chen, Y., S. Aulia, ..., B. L. Tang. 2006. AMIGO and friends: an emerging family of brain-enriched, neuronal growth modulating, type I transmembrane proteins with leucine-rich repeats (LRR) and cell adhesion molecule motifs. *Brain Res. Rev.* 51:265–274.
43. Sun, J., and R. MacKinnon. 2020. Structural basis of human KCNQ1 modulation and gating. *Cell.* 180:340–347.e9.
44. Shen, H., D. Liu, ..., N. Yan. 2019. Structures of human Nav1.7 channel in complex with auxiliary subunits and animal toxins. *Science.* 1308:1303–1308.
45. Thapa, P., R. Stewart, ..., J. T. Sack. 2021. EVAP: a two-photon imaging tool to study conformational changes in endogenous Kv2 channels in live tissues. *J. Gen. Physiol.* 153:1–24.
46. Fletcher-Taylor, S., P. Thapa, B. E. Cohen, ..., 2020. Distinguishing potassium channel resting state conformations in live cells with environment-sensitive fluorescence. *ACS Chem. Neurosci.* 11:2316–2326.
47. Tilley, D. C., K. S. Eum, ..., J. T. Sack. 2014. Chemoselective tarantula toxins report voltage activation of wild-type ion channels in live cells. *Proc. Natl. Acad. Sci. U S A.* 111:E4789–E4796.
48. Stewart, R., B. E. Cohen, and J. T. Sack. 2021. Fluorescent toxins as ion channel activity sensors. *Methods Enzymol.* 653:1–24.
49. Trapani, J. G., and S. J. Korn. 2003. Control of ion channel expression for patch clamp recordings using an inducible expression system in mammalian cell lines. *BMC Neurosci.* 4:15.
50. Liu, X., S. N. Constantinescu, ..., H. F. Lodish. 2000. Generation of mammalian cells stably expressing multiple genes at predetermined levels. *Anal. Biochem.* 280:20–28.
51. Mardinly, A. R., I. A. Oldenburg, ..., H. Adesnik. 2018. Precise multimodal optical control of neural ensemble activity. *Nat. Neurosci.* 21:881–893.
52. Lim, S. T., D. E. Antonucci, ..., J. S. Trimmer. 2000. A novel targeting signal for proximal clustering of the Kv2.1 K⁺ channel in hippocampal neurons. *Neuron.* 25:385–397.

53. Yu, S. P., and G. A. Kerchner. 1998. Endogenous voltage-gated potassium channels in human embryonic kidney (HEK293) cells. *J. Neurosci. Res.* 52:612–617.
54. Sack, J. T., and R. W. Aldrich. 2006. Binding of a gating modifier toxin induces intersubunit cooperativity early in the Shaker K channel's activation pathway. *J. Gen. Physiol.* 128:119–132.
55. Schoppa, N. E., and F. J. Sigworth. 1998. Activation of Shaker potassium channels. I. Characterization of voltage-dependent transitions. *J. Gen. Physiol.* 111:271–294.
56. Lopatin, A. N., E. N. Makhina, and C. G. Nichols. 1994. Potassium channel block by cytoplasmic polyamines as the mechanism of intrinsic rectification. *Nature.* 372:366–369.
57. Jara-Oseguera, A., I. G. Ishida, ..., L. D. Islas. 2011. Uncoupling charge movement from channel opening in voltage-gated potassium channels by ruthenium complexes. *J. Biol. Chem.* 286:16414–16425.
58. Chowdhury, S., and B. Chanda. 2012. Estimating the voltage-dependent free energy change of ion channels using the median voltage for activation. *J. Gen. Physiol.* 139:3–17.
59. Schindelin, J., I. Arganda-Carreras, ..., A. Cardona. 2012. Fiji: an open-source platform for biological-image analysis. *Nat. Methods.* 9:676–682.
60. Ponce, A., A. Castillo, ..., M. Cerejido. 2018. The expression of endogenous voltage-gated potassium channels in HEK293 cells is affected by culture conditions. *Physiol. Rep.* 6:e13663.
61. Gamper, N., J. D. Stockand, and M. S. Shapiro. 2005. The use of Chinese hamster ovary (CHO) cells in the study of ion channels. *J. Pharmacol. Toxicol. Methods.* 51:177–185.
62. Isom, L., K. De Jongh, ..., W. Catterall. 1992. Primary structure and functional expression of the beta 1 subunit of the rat brain sodium channel. *Science.* 256:839–842.
63. Isom, L. L., D. S. Ragsdale, ..., W. A. Catterall. 1995. Structure and function of the $\beta 2$ subunit of brain sodium channels, a transmembrane glycoprotein with a CAM motif. *Cell.* 83:433–442.
64. McEwen, D. P., and L. L. Isom. 2004. Heterophilic interactions of sodium channel beta 1 subunits with axonal and glial cell adhesion molecules. *J. Biol. Chem.* 279:52744–52752.
65. Kazarinova-Noyes, K., J. D. Malhotra, ..., Z. C. Xiao. 2001. Contactin associates with Na⁺ channels and increases their functional expression. *J. Neurosci.* 21:7517–7525.
66. Patino, G. A., L. R. F. Claes, ..., L. L. Isom. 2009. A functional null mutation of SCN1B in a patient with Dravet syndrome. *J. Neurosci.* 29:10764–10778.
67. Kirmiz, M., S. Palacio, ..., J. S. Trimmer. 2018. Remodeling neuronal ER–PM junctions is a conserved nonconducting function of Kv2 plasma membrane ion channels. *Mol. Biol. Cell.* 29:2410–2432.
68. Manders, E. M. M., J. Stap, ..., J. A. Aten. 1992. Dynamics of three-dimensional replication patterns during the S-phase, analysed by double labelling of DNA and confocal microscopy. *J. Cell Sci.* 103:857–862.
69. Gilchrist, J., S. Das, ..., F. Bosmans. 2013. Crystallographic insights into sodium-channel modulation by the $\beta 4$ subunit. *Proc. Natl. Acad. Sci. U S A.* 110:E5016–24.
70. Dunn, K. W., M. M. Kamocka, and J. H. McDonald. 2011. A practical guide to evaluating colocalization in biological microscopy. *Am. J. Physiol. Cell Physiol.* 300:C723–C742.
71. Cobb, M. M., D. C. Austin, ..., J. S. Trimmer. 2016. Cell cycle-dependent changes in localization and phosphorylation of the plasma membrane Kv2.1 K⁺ channel impact endoplasmic reticulum membrane contact sites in COS-1 cells. *J. Biol. Chem.* 291:5527.
72. Milesu, M., F. Bosmans, ..., K. J. Swartz. 2009. Interactions between lipids and voltage sensor paddles detected with tarantula toxins. *Nat. Struct. Mol. Biol.* 16:1080–1085.
73. Green, W. N., and O. S. Andersen. 1991. Surface charges and ion channel function. *Annu. Rev. Physiol.* 53:341–359.
74. Kajander, T., J. Kuja-Panula, ..., A. Goldman. 2011. Crystal structure and role of glycans and dimerization in folding of neuronal leucine-rich repeat protein AMIGO-1. *J. Membr. Biol.* 413:1001–1015.
75. Ednie, A. R., and E. S. Bennett. 2012. Modulation of voltage-gated ion channels by sialylation. *Compr. Physiol.* 2:1269–1301.
76. Ferrera, L., and O. Moran. 2006. $\beta 1$ -subunit modulates the Nav1.4 sodium channel by changing the surface charge. *Exp. Brain Res.* 172:139–150.
77. Johnson, D., M. L. Montpetit, ..., E. S. Bennett. 2004. The sialic acid component of the $\beta 1$ subunit modulates voltage-gated sodium channel function. *J. Biol. Chem.* 279:44303–44310.
78. Cohen, B. E., A. Pralle, ..., L. Y. Jan. 2005. A fluorescent probe designed for studying protein conformational change. *Proc. Natl. Acad. Sci. U S A.* 102:965–970.
79. Elinder, F., and P. Århem. 2003. Metal ion effects on ion channel gating. *Q. Rev. Biophys.* 36:373–427.
80. Broomand, A., F. Österberg, ..., F. Elinder. 2007. Electrostatic domino effect in the Shaker K channel turret. *Biophys. J.* 93:2307–2314.
81. Cerda, O., and J. S. Trimmer. 2011. Activity-dependent phosphorylation of neuronal Kv2.1 potassium channels by CDK5. *J. Biol. Chem.* 286:28738–28748.
82. Bar, C., M. Kuchenbuch, ..., R. Nabbout. 2020. Developmental and epilepsy spectrum of KCNB1 encephalopathy with long-term outcome. *Epilepsia.* 61:2461–2473.
83. Misonou, H., D. P. Mohapatra, ..., J. S. Trimmer. 2004. Regulation of ion channel localization and phosphorylation by neuronal activity. *Nat. Neurosci.* 7:711–718.
84. Baver, S. B., and K. M. S. O'Connell. 2012. The C-terminus of neuronal Kv2.1 channels is required for channel localization and targeting but not for NMDA-receptor-mediated regulation of channel function. *Neuroscience.* 217:56–66.
85. Mulholland, P. J., E. P. Carpenter-Hyland, ..., L. J. Chandler. 2008. Glutamate transporters regulate extrasynaptic NMDA receptor modulation of Kv2.1 potassium channels. *J. Neurosci.* 28:8801–8809.
86. Ikematsu, N., M. L. Dallas, ..., A. M. Evansc. 2011. Phosphorylation of the voltage-gated potassium channel Kv2.1 by AMP-activated protein kinase regulates membrane excitability. *Proc. Natl. Acad. Sci. U S A.* 108:18132–18137.
87. Delgado-Ramírez, M., J. J. De Jesús-Pérez, ..., A. A. Rodríguez-Menchaca. 2018. Regulation of Kv2.1 channel inactivation by phosphatidylinositol 4,5-bisphosphate. *Sci. Rep.* 8:1769.
88. Aréchiga-Figueroa, I. A., R. Morán-Zendejas, ..., A. A. Rodríguez-Menchaca. 2017. Phytochemicals genistein and capsaicin modulate Kv2.1 channel gating. *Pharmacol. Rep.* 69:1145–1153.
89. Park, K.-S., D. P. Mohapatra, ..., J. S. Trimmer. 2006. Graded regulation of the Kv2.1 potassium channel by variable phosphorylation. *Science.* 313:976–979.
90. Liu, R., G. Yang, ..., Y. Ding. 2016. Flotillin-1 downregulates K(+) current by directly coupling with Kv2.1 subunit. *Protein Cell.* 7:455–460.
91. David, J.-P., J. I. Stas, ..., E. Bocksteins. 2015. Auxiliary KCNE subunits modulate both homotetrameric Kv2.1 and heterotetrameric Kv2.1/Kv6.4 channels. *Sci. Rep.* 5:12813.
92. Li, X.-T., X.-Q. Li, ..., X.-Y. Qiu. 2015. The inhibitory effects of Ca²⁺ channel blocker nifedipine on rat Kv2.1 potassium channels. *PLoS One.* 10:e0124602.
93. Liu, X., Y. Fu, ..., B. R. Pattnaik. 2017. Potential independent action of sigma receptor ligands through inhibition of the Kv2.1 channel. *Oncotarget.* 8:59345–59358.
94. O'Connell, K. M. S., R. Loftus, and M. M. Tamkun. 2010. Localization-dependent activity of the Kv2.1 delayed-rectifier K⁺ channel. *Proc. Natl. Acad. Sci. U S A.* 107:12351–12356.
95. Aréchiga-Figueroa, I. A., M. Delgado-Ramírez, ..., A. A. Rodríguez-Menchaca. 2015. Modulation of Kv2.1 channels inactivation by curcumin. *Pharmacol. Rep.* 67:1273–1279.

96. Laedermann, C. J., N. Syam, ..., H. Abriel. 2013. β 1- and β 3- voltage-gated sodium channel subunits modulate cell surface expression and glycosylation of Nav1.7 in HEK293 cells. *Front. Cell. Neurosci.* 7:137.
97. Eichel, C. A., E. B. Ríos-Pérez, ..., G. A. Robertson. 2019. A micro-translatome coordinately regulates sodium and potassium currents in the human heart. *Elife.* 8:e52654.
98. Nagaya, N., and D. M. Papazian. 1997. Potassium channel alpha and beta subunits assemble in the endoplasmic reticulum. *J. Biol. Chem.* 272:3022–3027.
99. Gonzalez-Perez, V., X.-M. Xia, and C. J. Lingle. 2014. Functional regulation of BK potassium channels by γ 1 auxiliary subunits. *Proc. Natl. Acad. Sci. U S A.* 111:4868–4873.
100. Gonzalez-Perez, V., M. Ben Johny, ..., C. J. Lingle. 2018. Regulatory γ 1 subunits defy symmetry in functional modulation of BK channels. *Proc. Natl. Acad. Sci. U S A.* 115:9923–9928.
101. Wang, Y. W., J. P. Ding, ..., C. J. Lingle. 2002. Consequences of the stoichiometry of Slo1, α and auxiliary β subunits on functional properties of large-conductance Ca²⁺-activated K⁺ channels. *J. Neurosci.* 22:1550–1561.
102. Fox, P. D., R. J. Loftus, and M. M. Tamkun. 2013. Regulation of Kv2.1 K(+) conductance by cell surface channel density. *J. Neurosci.* 33:1259–1270.
103. Kirmiz, M., N. C. Vierra, ..., J. S. Trimmer. 2018. Identification of VAPA and VAPB as Kv2 channel-interacting proteins defining endoplasmic reticulum–plasma membrane junctions in mammalian brain neurons. *J. Neurosci.* 38:7562–7584.
104. Vierra, N. C., M. Kirmiz, ..., J. S. Trimmer. 2019. Kv2.1 mediates spatial and functional coupling of L-type calcium channels and ryanodine receptors in mammalian neurons. *Elife.* 8:e49953.
105. Johnson, B., A. N. Leek, ..., M. M. Tamkun. 2018. Kv2 potassium channels form endoplasmic reticulum/plasma membrane junctions via interaction with VAPA and VAPB. *Proc. Natl. Acad. Sci. U S A.* 115:E7331–E7340.
106. Frazzini, V., S. Guarnieri, ..., S. L. Sensi. 2016. Altered Kv2.1 functioning promotes increased excitability in hippocampal neurons of an Alzheimer’s disease mouse model. *Cell Death Dis.* 7:e2100.
107. Kimm, T., Z. M. Khaliq, and B. P. Bean. 2015. Differential regulation of action potential shape and burst-frequency firing by BK and Kv2 channels in substantia nigra dopaminergic neurons. *J. Neurosci.* 35:16404–16417.
108. Palacio, S., V. Chevaleyre, ..., J. S. Trimmer. 2017. Heterogeneity in Kv2 channel expression shapes action potential characteristics and firing patterns in CA1 versus CA2 hippocampal pyramidal neurons. *eNeuro.* 4:1–12.
109. Mandikian, D., E. Bocksteins, ..., J. S. Trimmer. 2014. Cell type-specific spatial and functional coupling between mammalian brain Kv2.1 K⁺ channels and ryanodine receptors. *J. Comp. Neurol.* 522:3555–3574.
110. Newkirk, G.S., D. Guan, ..., R.C. Foehring. 2021. Kv2.1 potassium channels regulate repetitive burst firing in extratelencephalic neocortical pyramidal neurons. *Cerebral Cortex* 2021,32:1055–1076.
111. Bishop, H. I., D. Guan, ..., J. S. Trimmer. 2015. Distinct cell- and layer-specific expression patterns and independent regulation of Kv2 channel subtypes in cortical pyramidal neurons. *J. Neurosci.* 35:14922–14942.
112. Murakoshi, H., and J. S. Trimmer. 1999. Identification of the Kv2.1 K⁺ channel as a major component of the delayed rectifier K⁺ current in rat hippocampal neurons. *J. Neurosci.* 19:1728–1735.
113. Guan, D., W. E. Armstrong, and R. C. Foehring. 2013. Kv2 channels regulate firing rate in pyramidal neurons from rat sensorimotor cortex. *J. Physiol.* 591:4807–4825.
114. Hodgkin, A. L., and A. F. Huxley. 1952. A quantitative description of membrane current and its application to conduction and excitation in nerve. *J. Physiol.* 117:500–544.